www.nature.com/scientificreports

SCIENTIFIC REPORTS

Assessing metastatic potential of breast cancer cells based on EGFR dynamics

Received: 15 June 2018
Accepted: 22 November 2018

Yen-Liang Liu[1], Chao-Kai Chou[2], Mirae Kim[1], Rohan Vasisht[1], Yu-An Kuo[1], Phyllis Ang[3], Cong Liu[1], Evan P. Perillo[1], Yu-An Chen[1], Katherine Blocher[1], Hannah Horng[4], Yuan-I Chen[1], Duc Trung Nguyen[1], Thomas E. Yankeelov[1,5,6,7,8], Mien-Chie Hung[2,9], Andrew K. Dunn[1] & Hsin-Chih Yeh[1,10]

Derailed transmembrane receptor trafficking could be a hallmark of tumorigenesis and increased tumor invasiveness, but receptor dynamics have not been used to differentiate metastatic cancer cells from less invasive ones. Using single-particle tracking techniques, we developed a phenotyping asssay named <u>T</u>ransmembrane <u>Re</u>ceptor <u>D</u>ynamics (TReD), studied the dynamics of epidermal growth factor receptor (EGFR) in seven breast epithelial cell lines and developed a phenotyping assay named <u>T</u>ransmembrane <u>Re</u>ceptor <u>D</u>ynamics (TReD). Here we show a clear evidence that increased EGFR diffusivity and enlarged EGFR confinement size in the plasma membrane (PM) are correlated with the enhanced metastatic potential in these cell lines. By comparing the TReD results with the gene expression profiles, we found a clear negative correlation between the EGFR diffusivities and the breast cancer luminal differentiation scores ($r = -0.75$). Upon the induction of epithelial-mesenchymal transition (EMT), EGFR diffusivity significantly increased for the non-tumorigenic MCF10A (99%) and the non-invasive MCF7 (56%) cells, but not for the highly metastatic MDA-MB-231 cell. We believe that the reorganization of actin filaments during EMT modified the PM structures, causing the receptor dynamics to change. TReD can thus serve as a new biophysical marker to probe the metastatic potential of cancer cells and even to monitor the transition of metastasis.

Receptor tyrosine kinases (RTKs) control many cell decision-making functions such as proliferation, survival, and movement. It has been shown that the important activities of RTKs are deregulated in most human cancers[1]. One form of the deregulation is the compromised spatial control and trafficking of RTKs[2]. While mounting evidence suggested that the derailed spatial regulation of RTKs could be a hallmark of tumorigenesis or even increased tumor invasiveness, very few reports studied the relationship between RTK dynamics and cancer cell behaviors. Grove's group studied the dynamics of EphA2 receptors and showed the clustering of EphA2 receptors is coupled with the increased invasiveness of cancer cells[3]. While this work demonstrated that subtle changes in the spatial organization of transmembrane receptors can lead to malignant cell behaviors, there is no attempt to use the receptor dynamics as a biophysical phenotyping method for cancer cells. By measuring the dynamics of RTKs, we believe it is possible not only to differentiate cancer cells with distinct malignant states but also monitor the transition from pre-malignant state to metastatic state.

Traditional phenotyping assays are based on molecular analyses of genomic, epigenetic, transcriptomic or proteomic biomarkers, which often suffer from the problems of high cost and large variation in today's single-cell

[1]Department of Biomedical Engineering, The University of Texas at Austin, Austin, TX, USA. [2]Department of Molecular and Cellular Oncology, The University of Texas MD Anderson Cancer Center, Houston, TX, USA. [3]Department of Electrical and Computer Engineering, The University of Texas at Austin, Austin, TX, USA. [4]Department of Bioengineering, The University of Maryland, College Park, MD, USA. [5]Institute for Computational Engineering and Sciences, The University of Texas, Austin, TX, USA. [6]Department of Diagnostic Medicine, Dell Medical School, The University of Texas at Austin, Austin, TX, USA. [7]Department of Oncology, Dell Medical School, The University of Texas at Austin, Austin, TX, USA. [8]Livestrong Cancer Institutes, The University of Texas at Austin, Austin, Texas, USA. [9]Center for Molecular Medicine and Graduate Institute of Cancer Biology, China Medical University, Taichung, Taiwan. [10]Texas Materials Institute, The University of Texas at Austin, Austin, TX, USA. Correspondence and requests for materials should be addressed to H.-C.Y. (email: Tim.Yeh@austin.utexas.edu)

analysis. To provide a multifaceted description of cancer cells, researchers have recently begun to explore physical properties of cancer cells (e.g., morphology[4], viscoelasticity[5], shear rheology[6], and motility[7]), with a hope to find an alternative way to quickly and precisely identify highly invasive cancer subtypes[8,9]. These physical science approaches have revealed dramatic differences in mechanics, migration, and adhesion between MCF10A (non-tumorigenic) and MDA-MB-231 (highly invasive) breast cell lines[8]. However, most of these physical interrogation methods have one or more of the following issues (SI Fig. S1): the need to physically touch the adherent cells using a special tool (e.g., a tip of atomic force microscopy (AFM)[5] or a micropipette aspiration device[10]), low information content (e.g., only one physical property, viscoelasticity, is measured in AFM), and low throughput (e.g., only one cell can be interrogated at a time by optical tweezers[11]). Currently, there is no physical interrogation technique that overcomes all of the above issues.

To address this challenge, we have developed a new biophysical phenotyping method termed **T**ransmembrane **Re**ceptor **D**ynamics (TReD), and showed that changes of TReD can be a signature of increased invasiveness. Our TReD phenotyping assay relies on an optical interrogation method (single-particle tracking of fluorescently tagged EGFRs) which not only avoids any physical manipulation of the cells but provides rich information about the receptors (e.g., transition probabilities between different diffusive states) and the microenvironment where the receptors are contained (e.g., confinement size). Here we demonstrate that EGFR dynamics, as an example of TReD, can be used to differentiate breast cell lines with distinct metastatic potential and monitor the epithelial-mesenchymal transition in the benign cell line. While our results agree well with the previous reports, our TReD assay is substantially easier than the current methods.

Results

TReD assay on the breast cell lines. To elucidate the connections among EGFR dynamics, PM compartmentalization, and invasiveness of cancer cells, we have performed the TReD assay on EGFRs in seven breast epithelial cell lines: MCF10A, MCF7, BT474, SKBR3, MDA-MB-468, MDA-MB-231, and BT549. EGFR was chosen in this study because its signaling network is compromised in many forms of human cancers[1,12]. In addition, EGFR can directly interact with actins[13,14], altering not only the EGF-EGFR binding affinity but also the EGFR dimerization kinetics[15,16]. We believe EGFR dynamics are coupled to the signaling networks through the local actin environment of the cancer cells, and changes in cancer cell behaviors, such as epithelial-mesenchymal transition, can alter the EGFR dynamics (Fig. 1A). Trajectories of 800-2,800 single EGFR complexes (termed FN-IgG-EGFR, as EGFRs were tagged with anti-EGFR IgG antibody-conjugated fluorescent nanoparticles, Fig. 1B)were analyzed per cell line using a modified mean-squared displacement (MSD) fitting algorithm[17,18], generating an averaged EGFR diffusivity (D) and a size of the linear confinement (L)[19] for each cell line (Fig. 1C,D). Based on the molecular classification of breast carcinoma[20,21], MCF10A is the benign, non-tumorigenic cell type(blue). In contrast, MDA-MB-231 and BT549 are the claudin-low, highly metastatic subtypes(red). MCF7 (luminal type A, light green), BT474 (luminal type B, green), SKBR3 (HER2-enriched, yellow) and MDA-MB-468 (basal type, orange) are the other four breast cancer subtypes with no to moderate *in vitro* metastatic potential[22]. The detailed clinicopathological features of the selected breast cell lines are listed in SI Table S1. From our TReD assay, we could clearly see that MDA-MB-231 and BT549 cells hadthe highest EGFR diffusivities (D) and the largest linear confinement sizes (L) (Fig. 1E,F). In particular, the EGFR diffusivity of MDA-MB-231 cell ($0.0112 \pm 0.0009\,\mu m^2/s$, n = 800; the statistical estimator represents sample mean ± standard error of the mean) was 38% and 37% higher than those of MCF10A ($0.0081 \pm 0.0004\,\mu m^2/s$, n = 2,598) and MCF7 ($0.0082 \pm 0.0004\,\mu m^2/s$, n = 2,686) cells, respectively (Fig. 1E). Although not as differentiable as diffusivity, L of MDA-MB-231 cell (99.3 ± 4.9 nm, n = 800) was 23% and 11% larger than those of MCF10A (80.5 ± 2.6 nm, n = 2,598) and MCF7 (89.8 ± 2.9 nm, n = 2,686) cells, respectively (Fig. 1F). Around 15–20 trajectories were collected from each single cell, and at least 50 cells were tested in one cell line. Although the EGFR dynamics cannot differentiate the cancerous MCF7 cell from the non-tumorigenic MCF10A cell, a clear discrimination of the MDA-MB-231 and BT549 cells (highly invasive) from the MCF7, BT474, SKBR3, and MDA-MB-468 cells (non- to less invasive) is a remarkable evidence that the changes of TReD can be a signature of increased cancer invasiveness.

Correlation between TReD and molecular signature. By comparing our TReD results with the luminal differentiation scores (LD scores)[23] of five distinct breast cancer subtypes (Fig. 2A), we found a clear negative correlation between the EGFR diffusivities and the LD scores (Pearson correlation $r = -0.75$, Fig. 2B). Calculated on the basis of UNC337 gene expression database (GSE18229 in GEO), the LD scores represent the potency of breast cells in a luminal epithelial differentiation lineage from mammary stem cells (MaSCs) to luminal progenitor cells, and eventually mature luminal cells[23,24], where a lower or more negative LD score represents a higher differentiation potential of the cell. As the EGFR diffusivities are clearly (negatively) correlated with the LD scores, we can potentially use TReD to replace LD scores in quantifying the differentiation potency of cancer cells. To identify key differences in the regulatory networks involved in cancer metastasis among these seven breast cell lines, we scrutinized their gene expression profiles published in the Genevestigator microarray database[25] (Fig. 2C and SI Tables S2 and S3). As expected, the gene expression patterns of the highly metastatic cells (claudin-low subtypes) showed signatures of EMT[26] and features of cancer stem cells[27,28]. The highly invasive cell lines, MDA-MB-231 and BT549, expressed an increased levels of EMT-upregulated genes at a high level(the purple box in Fig. 2C), in contrast to the basal- and luminal-type of cells which expressed luminal cell-related and EMT-downregulated genes at a high level. We thus hypothesized that our TReD phenotyping results can be influenced by the expression of EMT-upregulated genes. In other words, EMT might change the dynamics of EGFRs.

TReD assay monitors phenotypic transition of cells. To test the hypothesis that EMT can regulate the organization of cortical actin network and change the EGFR dynamics, we chemically induced EMT in three

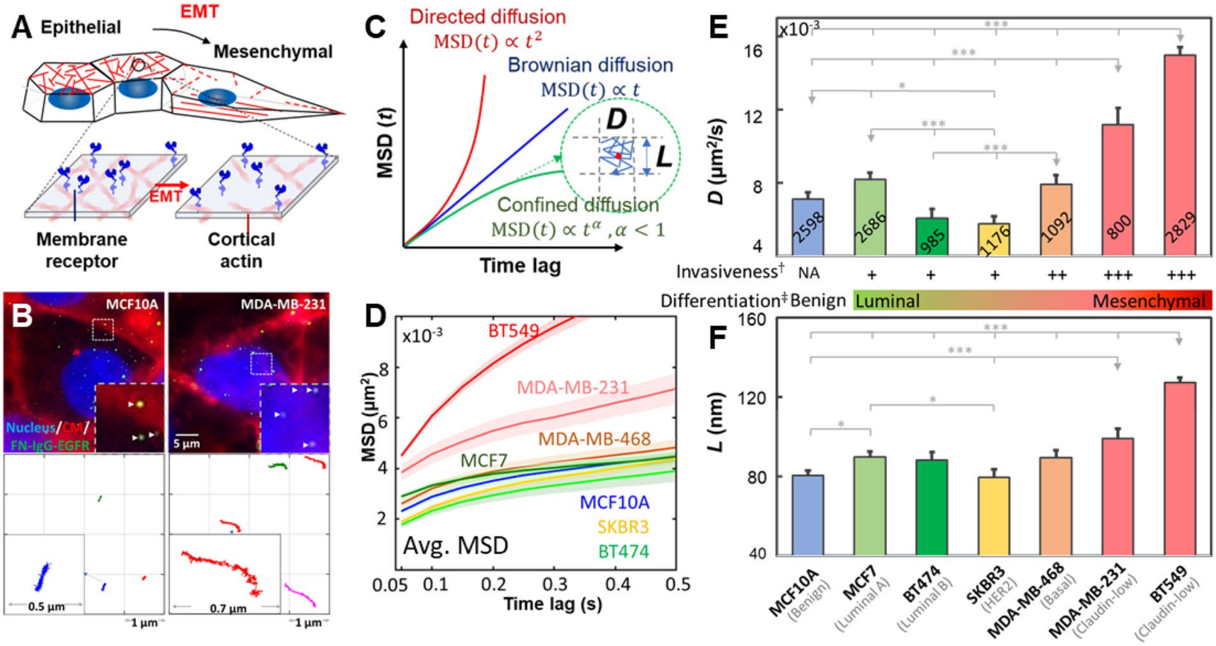

Figure 1. TReD, a new biophysical phenotyping method to assess metastasis. (**A**) Schematic shows the hypothetical effect of EMT on the EGFR dynamics. (**B**) Images of living cells and fluorescently labeled EGFRs (FN-IgG-EGFRs). The representative FN-IgG-EGFR trajectories shown in the lower panel were derived from the EGFRs pinpointed by the arrowheads. Individual trajectories were color-coded for identification. These trajectories were reconstructed from 60 seconds time-series images acquired in MCF10A and MDA-MB-231 cells. The insets are the zoom-in of trajectories. (**C**) The diffusivity of EGFR (*D*) and the linear size of the EGFR confinement (*L*) can be extracted from trajectories using a modified MSD fitting algorithm. (**D**) Averaged-MSD curves from 800–2,800 trajectories acquired in the seven breast epithelial cell lines. The solid line and the ribbon represent mean value and standard error of the mean, respectively. (**E**,**F**) Characterization of EGFR diffusivity (*D*) and compartment size (*L*) among these seven breast cell lines. More invasive breast cancer cell lines exhibit higher EGFR diffusivities and larger compartment sizes. The number of trajectories collected from each cell line is shown on each bar. Statistical comparison was performed using unpaired t-test., where the asterisk represents statistical significance: ***$p < 0.001$, **$p < 0.01$, *$p < 0.05$. The error bar represents the standard error of the mean. †*In vitro* invasiveness was derived from Lin's report[22]. ‡Luminal differentiation scores of breast cancer cells were derived from the Perou[23] and the Partanen[24] reports.

breast cell lines (non-tumorigenic MCF10A, non-invasive MCF7, and highly invasive MDA-MB-231) using the commercial EMT induction medium (StemXVivo EMT Inducing Media Supplement) (Fig. 3A–C) and measured TReD before and after the induction (Fig. 3D,E). The effectiveness of EMT induction was verified by an EMT immunochemistry kit (SC026, R&D systems) which identifies snail, vimentin, and E-cadherin (Fig. 3A) and imaged with a Structured Illumination Super-Resolution Microscope (SR-SIM). In EMT-induced MCF10A and MCF7 cells, the decrease of E-cadherin (pointed by the arrowheads in Fig. 3A) resulted in reduced intercellular adhesion and increased cell motility[29]. In addition, upon EMT induction, cadherins could incidentally establish a link with the actomyosin cytoskeleton through α- and β- catenin, and a decrease of cadherin-containing cell-cell junctions could reduce cortical tension and increase actin turnover[30]. As a result, we observed clear morphological transformations in EMT-induced MCF10A and MCF7 from squamous cells to spindle-shaped cells which expressed less cortical actin but more stress fibers (Fig. 3B). In tumor progression, cells that undergo EMT reorganize their cortical actin cytoskeleton into stress fibers or membrane projections, which enables dynamic cell elongation and directional motility[31–33]. The EMT-induced MCF10A clearly exhibited actin-rich membrane projections that facilitate cell movement and act as sensory extensions of the cytoskeleton (pointed by the arrows in Fig. 3B). These projections included lamellipodia (sheet-like membrane protrusions) and filopodia (spike-like extensions) at the edge of lamellipodia[34]. In particular, the actin-rich invadopodia could exert a proteolytic function in extracellular matrix degradation, facilitating cell invasion[34]. As MCF10A and MCF7 cells became similar to MDA-MB-231 cell after EMT induction, we expected to see higher EGFR diffusivities and larger linear confinement sizes. Indeed, EMT-induced MCF10A and MCF7 cells showed a marked increase in EGFR diffusivities ($0.0139 \pm 0.0012\,\mu\mathrm{m}^2/\mathrm{s}$, $n = 651$; $0.0111 \pm 0.0010\,\mu\mathrm{m}^2/\mathrm{s}$, $n = 713$), which were substantially higher (99% and 56%) than those of the untreated controls ($0.0070 \pm 0.0005\,\mu\mathrm{m}^2/\mathrm{s}$, $n = 1361$; $0.0071 \pm 0.0006\,\mu\mathrm{m}^2/\mathrm{s}$, $n = 1{,}050$) (Fig. 3D). In contrast, the MDA-MB-231 cell showed a decrease in EGFR diffusivity (0.0106 ± 0.0016, $n = 331$ to $0.0081 \pm 0.0009\,\mu\mathrm{m}^2/\mathrm{s}$, $n = 315$) after EMT induction (by 23%, but without a statistical significance). On the other hand, the membrane compartment size (*L*) increased in all three cells after EMT induction, although the changes were less statistically significant for MCF7 and MDA-MB-231 cells (Fig. 3E). We emphasize that the highly invasive cells possess the features of mesenchymal cells, as MDA-MB-231 and BT549 cells express a high

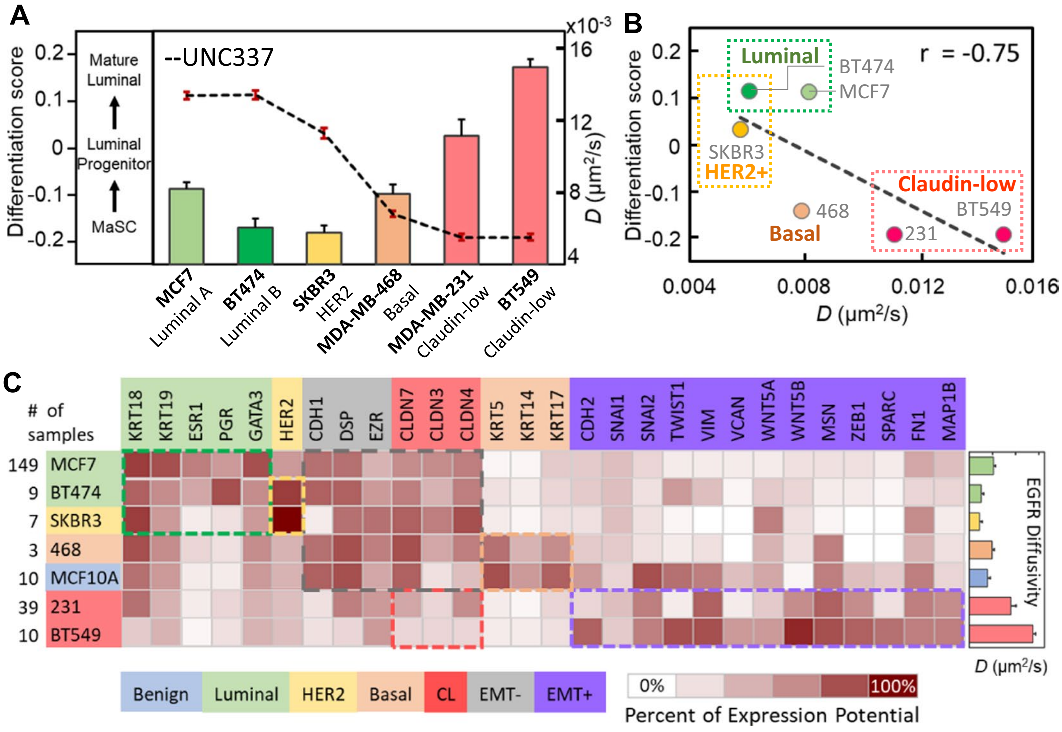

Figure 2. Correlation between TReD and molecular signature. (**A**) EGFR diffusivity versus luminal differentiation score. The luminal differentiation scores, as calculated on the basis of UNC337 gene expression database, represent the differentiation potentials of breast cells in a luminal epithelial differentiation lineage from mammary stem cells (MaSCs) to the luminal progenitor cells, and eventually to mature luminal cells. (**B**) The negative correlation between EGFR diffusivity and luminal differentiation score was seen, with the Pearson correlation coefficient $r = -0.75$. (**C**) Heat map generated from Genevestigator, showing the expression potential of the 28 genes related to EMT and the five breast cancer cell subtypes (luminal A, luminal B, HER2-rich, basal, and claudin-low). The highly invasive cancer cells exhibit features of mesenchymal cells. As higher EGFR diffusivities were observed in the highly invasive cells (MDA-MB-231 and BT549), we speculated that the EMT might alter the EGFR dynamics. Each cell subtype and the corresponding biomarkers have the same color code, and the colored boxes highlight the differences in molecular signatures among these seven cell lines. The *CLDN* genes are the biomarkers for claudin-low cells but also the EMT-downregulated genes.

level of EMT-upregulated genes (Fig. 2C). The results of our EMT induction studies (Fig. 3) resonated well with the cell line studies (Fig. 1). TReD assay can, therefore, probe the transition of cells from the pre-malignant state to the highly invasive state.

TReD assay provides detailed information about the receptors. The histograms of log *D* and log *L* revealed the detailed information on the heterogeneity of EGFR dynamics and the change of EGFR dynamics upon EMT (Fig. 4). The log *D* plot clearly showed three diffusive states (immobile, less mobile, and mobile states) for the three cell lines (Fig. 4A), and EMT induction changed the profiles of three-component Gaussian fits. It is well known that the dynamic properties of single member receptors often vary in a wide range of spatial scales (from tens to hundreds of nanometers) and temporal scales (from a few milliseconds to seconds)[35,36]. This complex behavior is caused by a combination of factors[37], including molecular crowding[38], molecular interactions[16,39], membrane topology[40], and interactions with nanostructures within the membrane domains (e.g., caveolae[41,42], clathrin-coated pits[43], lipid rafts[44], and cytoskeleton corrals[35,45–47]). The MCF10A and MCF7 cells had their mobile-state diffusivities substantially increased (blue dash lines, 117% & 67%, respectively), but the mobile-state diffusivity of MDA-MB-231 cell decreased after EMT induction (45%). On the other hand, the log *L* histograms of the benign (MCF10A) and the non-invasive (MCF7) cells, once fitted with a two-component Gaussian model, showed a substantial increase for the smaller *L* component after EMT induction (red dash lines, by 56% & 93%, Fig. 4B). However, such a significant increase in the linear confinement size was not seen in the highly invasive cell (MDA-MB-231). We noted that the average track duration for a single EGFR complex was about 30 seconds (all tracks shorter than 15 s were discarded) and within 30 seconds the EGFR complex could have switched among different diffusive states multiple times (especially for MCF10A and MCF7 cells). We have previously observed an interchange of four diffusive states of EGFR (Brownian diffusion, confined diffusion, directed diffusion, and immobilization) in A431 cells (upon EGF stimulation; here all of the experiments were done without EGF stimulation) using a 3D-SPT technique[19]. We emphasize that other physical science approaches provide no detailed description of the receptor motion and the microenvironment where the receptors are contained, and shed no light on how the receptor behavior can change during the phenotypic transition. Based on the evidence that both

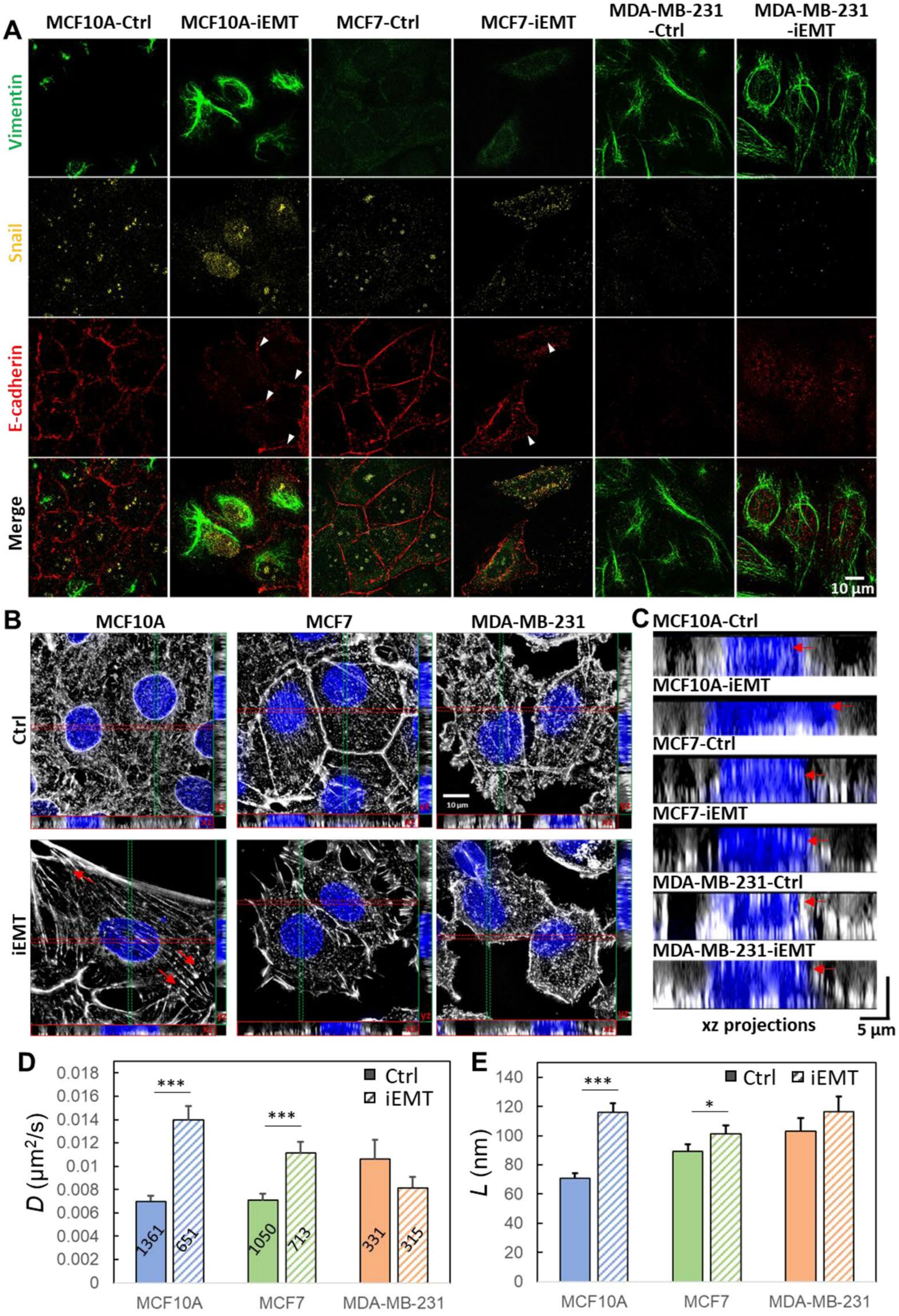

Figure 3. Characterization of EMT-induced cells and EGFR dynamics. (**A**) The phenotypes of the MCF10A, MCF7, and MDA-MB-231 cells treated with/without EMT induction medium (Ctrl and iEMT) were verified using immunocytochemistry with two mesenchymal biomarkers (snail and vimentin) and an epithelial biomarker (E-cadherin). As expected, after EMT induction, the mesenchymal biomarkers were up-regulated, while the epithelial biomarker was downregulated in both MCF10A and MCF7 cells (lower levels of E-cadherin pointed by the arrowheads). On the other hand, the expression levels of these three biomarkers in MDA-MB-231 cells remained the same before and after EMT induction, which reflects the fact that MDA-MB-231 is already a mesenchymal cell type. Scale bar represents 10 µm. (**B**) SR-SIM images of cortical actin. Maximum intensity projection on the xy plane, and orthogonal cross-sections (xz and yz) of MDA-MB-231, MCF7, MCF10A cells before and after EMT-induction. EMT induction clearly transformed the morphology of MCF10A and MCF7 cells (from the squamous shape to the spindle shape) and reorganized actin filaments (less cortical actins but more stress fibers). Having more stress fibers at the basal side of these chemically treated MCF10A and MCF7

cells indicated that these epithelial cells acquire fibroblast-like properties – a signature of EMT. The F-actin was labeled with Alexa Fluor 633 Phalloidin, and the nuclei were stained with Hoechst 33258. Scale bar represents 10 µm. (**C**) XZ projections of the SR-SIM images. The yellow dashed lines represent the apical borders of cells. (**D**,**E**) *D and L* were extracted from EGFR trajectories acquired from these cells. EMT-induction clearly facilitated the diffusion of EGFR in MCF10A and MCF7 cells (epithelial) but had no significant impact on MDA-MB-231 cell(mesenchymal). The number of trajectories analyzed is labeled on each bar in (D). Statistical comparison was performed using unpaired t-test, where the asterisk represents statistical significance ***$p < 0.001$, **$p < 0.01$, *$p < 0.05$. The error bar represents the standard error of the mean.

the mobile-state EGFR diffusivities and the nanoscopic confinement sizes increased after EMT induction, we concluded that the cortical actin network was reorganized during EMT.

Depolymerization of F-actin increases EGFR diffusivity and enlarges confinement size in benign cells. To investigate how the cortical actin structure might influence EGFR dynamics, we treated the three cell lines with Latrunculin B (Lat-B) that depolymerizes F-actin[48]. Before treatment, MCF10A and MCF7 cells were featured by abundant peri-junctional actin bands (pointed by arrowheads in Fig. 5A) and denser cortical actin networks in their apical PM (Fig. 5B). In contrast, MDA-MB-231 cell exhibited many filopodia-like structures (pointed by arrows in Fig. 5A). Upon Lat-B treatment, substantial disruption of stress fibers, reduction of cortical actin, retraction of filopodia, and decrease in projected cell area were observed in all three cell lines (Fig. 5A). The XZ projections clearly showed the dissociation of cortical actin from the apical surface of the PM after treatment (Fig. 5B). This reorganization of cortical actin meshwork was clearly responsible for the increased diffusivity of EGFR(Fig. 5C) and the enlarged confinement size (Fig. 5D) in the Lat-B-treated MCF10A cells. While Lat-B also depolymerized the F-actin in MCF7 cells, especially at the cell-cell contact (Fig. 5A), the change in EGFR diffusivity was marginal (Fig. 5C). Interestingly, the Lat-B treatment did not affect the EGFR diffusivity in MDA-MB-231 cell. The log *D* and log *L* histograms of the Lat-B treated cells are shown in SI Fig. S2.

EMT-induced actin reorganization suppresses EGF-dependent tyrosine phosphorylation in MCF10A cell. Many studies have demonstrated that spatiotemporal confinement of the membrane receptors facilitates oligomerization of the membrane receptors and their associated molecules[16,49] and further enhances signaling in the compartment[3,35,50,51]. Therefore, we speculated whether the EMT-induced actin reorganization would impact EGFR phosphorylation. Here we focused on MCF10A cell and estimated the level of EGFR phosphorylation using a commercial kit (Phospho-EGFR Cellular Assay, Cat. # 64EG1PEG, cisbio) at 6 different time points after EGF stimulation (0 s, 15 s, 30 s, 60 s, 120 s, and 300 s). Starting from time zero (EGF stimulation), we also tracked EGFR dynamics for 100 seconds (Fig. 6A). We found that the EGFR phosphorylation levels in the EMT-induced MCF10A cell (with less EGFR confinement) were indeed lower than those in the untreated cells over the course of 5 minutes (Fig. 6B), suggesting that EGFRs might have become desensitized. To reveal the connection between EGFR phosphorylation and EGFR dynamics, we use an analytical tool, variational Bayes single-particle tracking (vbSPT)[52], to characterize the transitions between different EGFR diffusive states (Fig. 6C). vbSPT identified three diffusive states (immobile, less mobile, and mobile) and provided state occupancies and transition probabilities among states. We found EMT induction greatly suppressed the transition probability from the mobile to the less mobile state ($P_{Mobile \rightarrow Less\ mobile}$) after EGF stimulation (Fig. 6C and 6D), which agreed well with our previous observation that EMT induction relaxed the physical confinement of EGFR, leading to a higher overall EGFR diffusivity. Together, we concluded that EMT-induced actin reorganization enlarges the meshwork confinements, thus reducing EGF-dependent tyrosine phosphorylation (Fig. 6E). The increase in *D* and *L* and the decrease in $P_{Mobile \rightarrow Less\ mobile}$ also suggest less EGFR dimerization and less association between EGFR and actin proteins after EMT.

Discussion

To the best of our knowledge, transmembrane receptor dynamics (TReD) have never been used to distinguish cancer cells with distinct metastatic potentials. We followed the structure-property-function-disease paradigm proposed by Suresh[53] and established connections among EGFR dynamics, cancer metastasis, EMT, cortical actin structures, and EGFR phosphorylation. Here we demonstrate that EGFR dynamics can serve as a physical biomarker to distinguish highly-invasive breast cancer cells (MDA-MB-231 and BT549) from other subtypes (Fig. 1), to monitor phenotypic transition of cells (e.g., EMT in MCCF10A, Fig. 3D), and to probe the changes in the cellular microenvironment (reorganization of cortical actin meshwork in Fig. 3E). As mechanical force, spatial organization of surface receptors, and receptor-mediated signal transduction (which leads to increased metastatic potential) are all coupled[3], chemical states of the cell can influence the physical states of the cell and vice versa[54,55], which lay the foundation of our TReD assay.

There are many benefits of using TReD to monitor the alteration of cell propeties, such as cytoskeletal changes and mechanical propety changes. While the cytoskeletal changes can be directly visualized by methods such as structured illumination microscopy, tedious cell fixation and staining with external fluorophores (e.g., Alexa-633 Phalloidin) are often needed. TReD, in contrast, provides a quick and simple way to evaluate cytoskeletal changes in live cells. While the mechanical properties of cancer cells can be measured by AFM[5] or micropipette aspiration[10], the requirement to physically touch the cells makes these methods incompatible with typical microfluidic devices. On the contrary, TReD is based on single-particle tracking that can be easily performed in many commercially available microfluidic cell-sorting devices (e.g., *Parsortix* from Angle PLC for CTC isolation[56], SI Fig. S3). In this report, we focus on two physical parameters (*D* and *L*) that most successfully distinguish

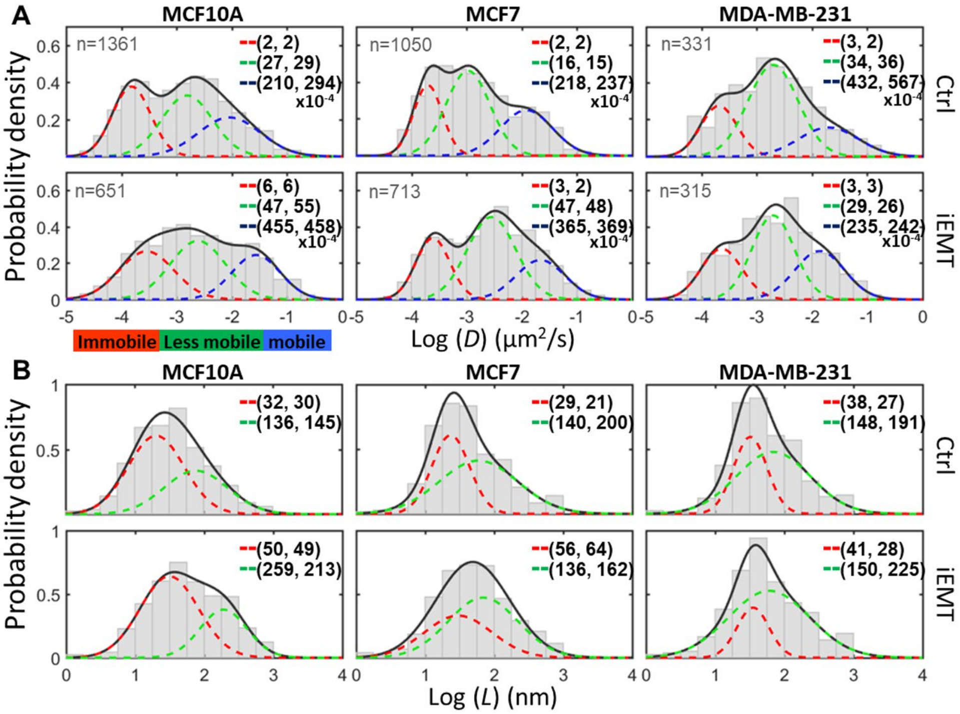

Figure 4. EMT changes the diffusivity of EGFR and the size of microdomains. Histograms of log *D* (**A**) and log *L* (**B**) extracted from EGFR trajectories. The histograms reveal the heterogeneity of EGFR dynamics and the change of EGFR dynamics upon EMT. EMT induction clearly reshaped the population distributions among the three different diffusive states (immobile, less mobile, and mobile). In MCF10A and MCF7 cells, both EGFR diffusivities and the compartment sizes increased after EMT induction. The values shown in the histograms represent the arithmetic moments of *D* or *L* ((arithmetic means ($\overline{X}$), arithmetic standard deviations($\sigma_{\overline{x}}$))) derived from Gaussian mixture model fitting of log *D* and log *L* (with 3 or 2 sub-populations). The three subpopulations are defined as immobilization (red), less mobile (green), and mobile (blue). The number of trajectories analyzed from each group is shown in (**A**).

the malignant subtypes (MDA-MB-231 and BT549) from the other subtypes, while the discrimination among non- to less-invasive subtypes is currently marginal. However, we emphasize that much more information about the receptors, such as endocytosis process, active transport, and dimerization kinetics, can be acquired using more sophisticated 3D-SPT techniques[57–61] or two-color colocalization techniques[16,62,47,58]. Although we have previously advanced 3D-SPT techniques[63] and reported a wealth of information about EGFR trafficking, from PM to cytosol, in skin cancer A431 cells[19], 3D-SPT is currently limited by its low throughput (tracking one receptor complex at a time). Bypassing this low throughput issue, here we demonstrate the TReD assay based on 2D-SPT. Our next goal is to extend TReD assay from 2D to 3D and incorporate more dynamical parameters that can further differentiate the four non- to less-invasive subtypes (MCF7, BT474, SKBR3, and MDA-MB-468). In addition, we are also aware that cross-linking effect from IgG antibodies or multivalent nanoparticles could have impacted EGFR dynamics. Therefore, using advanced monovalent nanoparticles[64,65] for tracking of single receptors is excepted to improve the performance of TReD assay.

We notice that the HER2-positive breast cancer cells, BT474 and SKBR3, had the lowest EGFR diffusivities among all seven cell lines tested in Fig. 1E. This result resonates with Agazie's report that overexpression of *HER2* stabilizes HER2 homodimers and HER2-EGFR heterodimers[66]. Following ligand binding, the EGFR family receptors (EGFR/HER1/ErbB-1, HER2/ErbB-2/neu, HER3/ErB-3, and HER4/ErbB-4) interact to form an array of homo- and heterodimers[67]. In particular, in cells expressing both EGFR and HER2, ligand stimulation induces both EGFR-EGFR homodimerization and EGFR-HER2 heterodimerization[68]. The activated dimers further recruit binding proteins to enhance signaling[2,69], thus resulting in a bigger EGFR complex with reduced diffusivity[51]. To assess the correlation between the expression levels of EGFR family receptors and EGFR dynamics, we analyzed the gene expression data of the four EGFR family receptors (*EGFR*, *HER2*, *HER3*, and *HER4*) and compared that to the EGFR diffusivity (Fig. S4). Interestingly, we found no strong correlation between EGFR diffusivity and EGFR expression level ($r = -0.05$). In contrast, the *HER2* and *HER3* gene expression levels are clearly negatively correlated with EGFR diffusivity ($r = -0.6$ and $r = -0.67$, respectively). We emphasize that, although interesting, this result needs to be reconfirmed in isogenic cell models where the expression levels of each EGFR family receptor are well-controlled and characterized, such as conducting EGFR tracking in a genetically modified MCF10A cell with a well-regulated HER2 expression level.

Many research groups have demonstrated that the cortical actin compartmentalizes the PM into microdomains (~40–300 nm in diameter[70]) which temporally confine transmembrane receptors from a few milliseconds to hundreds of milliseconds. This spatiotemporal confinement facilitates oligomerization of the receptors and

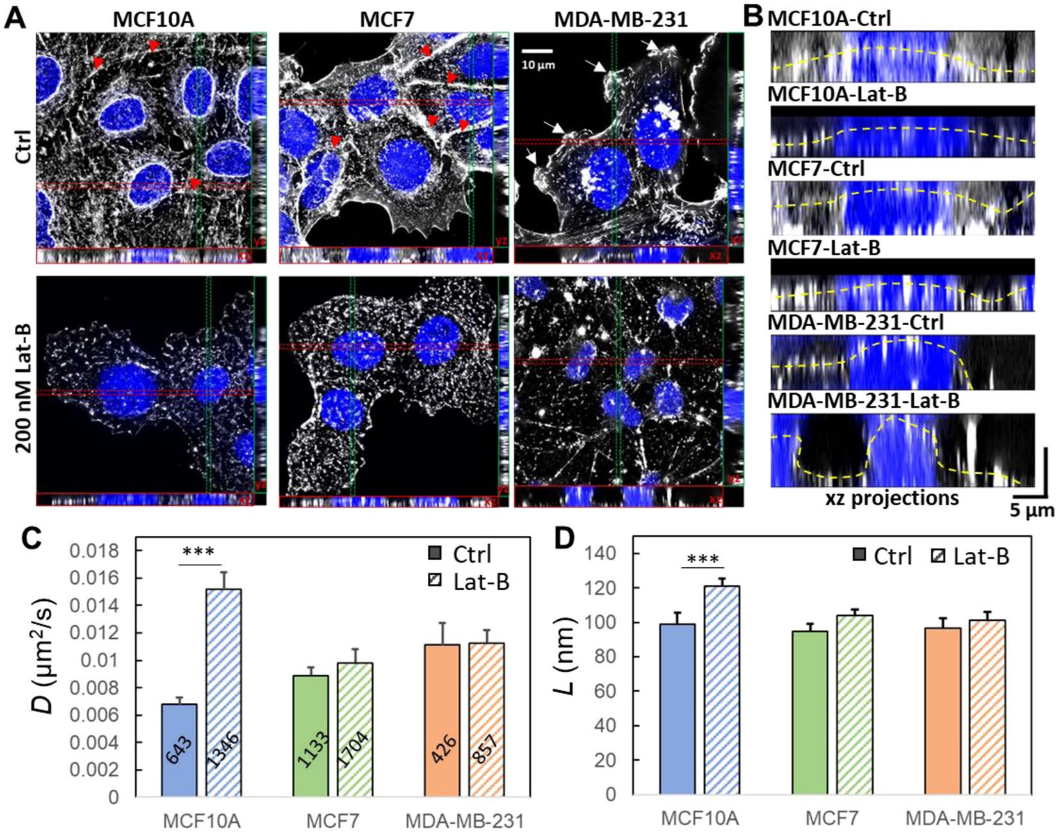

Figure 5. Depolymerization of F-actin increases EGFR diffusivity and enlarges confinement size. (**A**) Maximum intensity projection on the xy plane, and orthogonal cross-sections (xz and yz) of MDA-MB-231, MCF7, and MCF10A cells before and after Lat-B treatments. Lat-B indeed inhibited the polymerization of F-actin. The red arrowheads indicate the peri-junctional actin bands, while the white arrows pinpoint the filopodia-like structures. (**B**) The xz projections clearly show the dissociation of cortical actin from the apical surface of the plasma membrane after the treatment. The yellow dashed lines represent the apical borders of cells. (**C**) Diffusivities of EGFR extracted from trajectories. (**D**) Linear dimension of the confinement extracted from trajectories. The number of trajectories analyzed is labeled on each bar in (**C**). Statistical comparison was performed using unpaired t-test, where the asterisk represents statistical significance: $^{***}p < 0.001$, $^{**}p < 0.01$, $^{*}p < 0.05$. The error bar represents the standard error of the mean.

their associated molecules[16,49] and enhances signaling in the microdomains[3,35,50,51]. We have shown that EMT relaxes the EGFR confinement (Fig. 2), which decreases the oligomerization of receptors and results in a lower level of tyrosine phosphorylation (Fig. 6). However, we emphasize that spatial confinement of transmembrane receptors does not always enhance signaling. For instance, cortical actin can also act as barriers to prevent receptor oligomerization, restricting the antigen-stimulated signaling in immune cells[71,72]. In other words, cortical actin could have two distinct effects in regulating membrane receptor signaling. On one hand, it may facilitate the clustering of receptors and downstream effectors to enhance cell signaling. On the other hand, it can separate receptors from each other and prevent the initiation of cell signaling. In addition to the confinement size, what also plays a critical role here is the number of receptors in each confinement (i.e., the expression level of receptors). As mentioned above, future TReD assay will collectively characterize confinement size, receptor diffusivity, and receptor density on the PM in differentiating cancer subtypes. Other than the physical constraints from the intracellular domain, the extracellular matrix can also modulate the dynamics of transmembrane proteins. Grinstein's group has recently demonstrated that extracellular matrix regulates the dynamics of transmembrane proteins such as CD44 and Fcγ receptor[73]. We are adapting the TReD assay to study *in vivo* models through intravital microscopy, which will shed light on how extracellular matrix, interstitial fluid, and cell-cell interactions affect receptor dynamics.

In conclusion, we present a new type of biophysical phenotyping assay - termed TReD which is capable of differentiating the highly-invasive cancer cell lines (MDA-MB-231 and BT549) from the non- to less-invasive cancer cell lines. Through the combined interpretation of TReD and structured illumination microscopy images, we show that EMT reorganizes cortical actin and modulates the dynamics of EGFRs. Finally, we demonstrate that the EMT relaxes the confinement of EGFRs and attenuates the EGF-induced tyrosine phosphorylation of EGFR. However, the detailed mechanism of how the cortical cytoskeleton serves as a guardian to upregulate or downregulate cell signaling remains to be answered. We envision that a collective, systematic investigation on (i) the

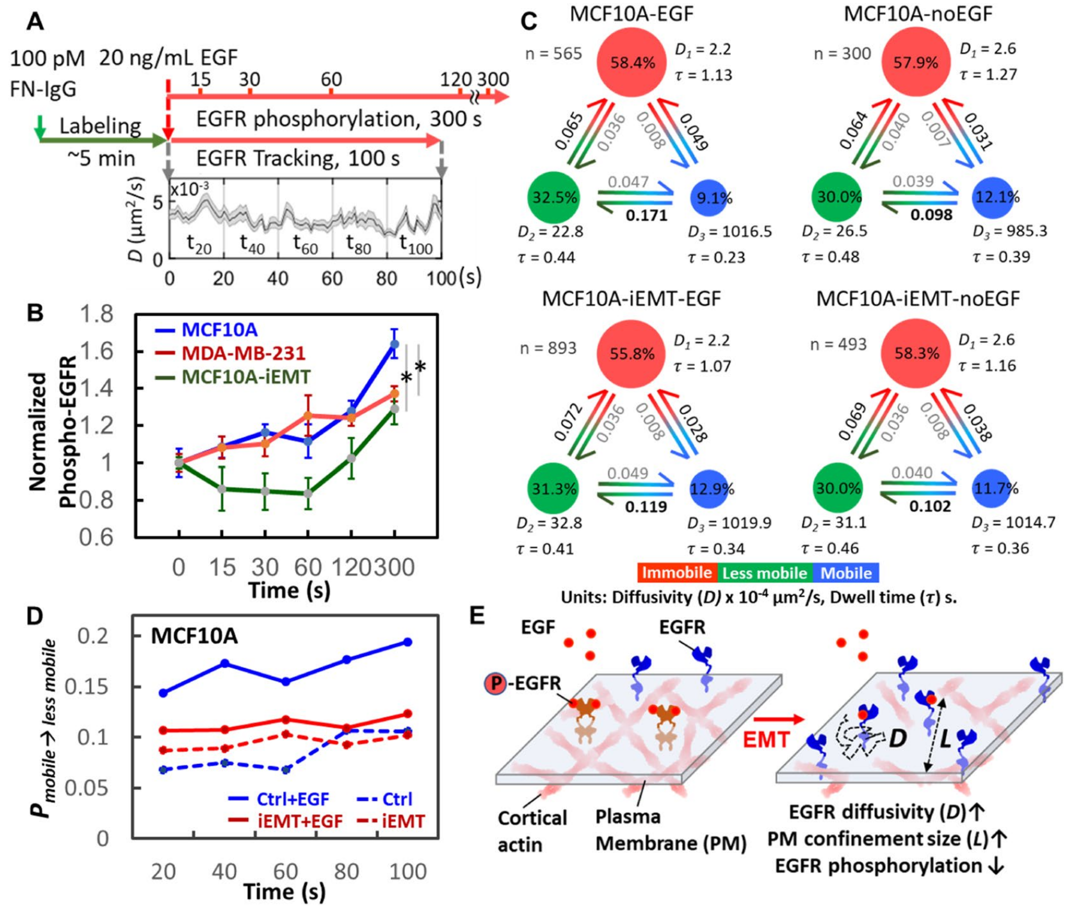

Figure 6. Relaxation of EGFR confinement reduced EGF-induced EGFR phosphorylation. (**A**) Procedure to evaluate the connection between EGFR dynamics and EGFR phosphorylation. For EGFR phosphorylation, cells were stimulated with or without EGF ($t = 0$ s), and the phosphorylation was measured at different time points. EGFR tracking was immediately initiated after the addition of cell culture medium containing EGF. The plot shows the time trace of EGFR diffusivity. (**B**) EGF-stimulated EGFR phosphorylation in MCF10A, EMT-induced MCF10A, and MDA-MB-231 cells. Three trials were conducted. In each trial, 4 data points were collected at one time point. Statistical comparison was performed using unpaired t-test, where the asterisk represents statistical significance: $^*p < 0.05$. The error bar represents the standard error of the mean. (**C**) vbSPT analysis revealed the dynamics of EGFRs in MCF10A cell under the perturbation of EMT-induction or EGF-stimulation. The three diffusive states are defined as immobilization (red), less mobile (green), and mobile (blue).Transition probabilities, state occupancies, average dwell time (τ), and number of trajectories analyzed are shown in each subplot. (**D**) The transition probability from the mobile to the less mobile ($P_{Mobile \to Less\ mobile}$). Trajectories were truncated into five time windows and analyzed by vbSPT to reveal the changes of $P_{Mobile \to Less\ mobile}$ every 20 s. (**E**) Schematic shows our hypothesis of the effect of EMT on the dynamics of EGFRs and EGFR phosphorylation.

compartmentalization of PM in single cells and (ii) the density and dynamics of receptors in single compartments across a variety of cells wouldelucidate the role of the cortical cytoskeleton in transmembrane signaling.

Methods

Cell culture.

Used as the model systems, BT474, SKBR3, MDA-MB-468, MDA-MB-231, and BT549 cells were grown in DMEM/F12 medium (11320082, Thermo Fisher Scientific) supplemented with 10% fetal bovine serum (16140071, Thermo Fisher Scientific) and 50 U/mL penicillin-streptomycin (15070063, Thermo Fisher Scientific). MCF7 was grown in MEM (11095-080, Thermo Fisher Scientific) supplemented with 10% fetal bovine serum and 50 U/mL penicillin-streptomycin. The benign breast epithelial cell line, MCF10A, was maintained as described[69]. Please see SI Method S1 for a detailed description of cell culture.

EMT induction and depolymerization of actin filaments.

To induce EMT, MCF10A, MCF7, and MDA-MB-231 cells were grown in their original media that were additionally supplemented with the EMT induction supplement (StemXVivo EMT Inducing Media Supplement, Cat. No. CCM017, R&D systems) for five days[74]. The supplement includes anti-human E-cadherin, anti-human sFRP-1, anti-human Dkk-1, recombinant human Wnt-5a, and recombinant human TGF-β. The cells were characterized by an EMT immunochemistry kit (SC026, R&D systems) which contains three types of IgGs targeting snail, E-cadherin, and vimentin, respectively.

Latrunculin B (Lat-B, ab144291, Abcam) was used to depolymerize actin filaments[48]. For Lat-B-treated cells, cells were incubated with 200 nM Lat-B supplemented in serum-free DMEM/F12 or MEM medium for 10 min.

Fluorescent probe labeling to EGFR. Anti-EGFR IgG antibody-conjugated fluorescent nanoparticles (FN-IgG) were used to label EGFR for tracking. The FN-IgG probe was prepared as described by us previously[19]. Full details of fluorescently labeling EGFR can be found in SI Method S2.

Single-particle tracking and trajectory analysis. Wide-field imaging for SPT is performed using an Olympus IX71 inverted microscope equipped with a 60x 1.2 N.A. water objective (UPLSAPO 60XW, Olympus). All imaging was conducted at 37 °C using a temperature-controlled stage (Stable Z System, Bioptechs). Wide-field excitation was provided by a metal halide lamp with a 545/25 nm BP excitation filter. Emission was collected by a Scientific CMOS camera (ORCA-Flash4.0) through 565 nm dichroic and 605/70 BP. The pixel size is equivalent to 107 nm. Images of FN-IgG tagged EGFRs (FN-IgG-EGFRs) were acquired at 20 frames per second for a total of 1,200 frames (TReD assay) or 2,000 frames (EGF-stimulation). The analysis of the acquired image series was performed as described previously[47,75] to obtain trajectories (SI Method S3). The SPT software was a gift from Prof. Keith Lidke at the University of New Mexico. The trajectories were analyzed using MSD analysis to extract the EGFR diffusivity (D) and the linear size the confinement (L). To reveal the multiple transitions of EGFRs among the distinct diffusive states, trajectories were further analyzed with variational Bayes SPT (vbSPT)[52] to identify the number of diffusive states and the state transition probabilities. Please see supplementary information for detailed descriptions of single-particle tracking (SI Method S4) and trajectory analysis (SI Method S5).

Gene expression analysis of breast cancer cell microarray dataset. The luminal differentiation predictor was developed by Perou group[24] and trained with the database GSE16997 which is contributed by Partanen group[23]. Then this predictor was applied to the UNC337 database (GSE18229 in GEO) to calculate the luminal differentiation scores (LD scores) of 39 tumor samples ($n = 337$). The calculation of LD score is described in SI Method S6. A search engine for gene expression, Genevestigator[25], was used to identify the gene expression patterns of these selected cell lines in a large scale, and 26 datasets and 28 genetic markers were included in the analysis. For data selection, we selected the gene expression data of these seven cell lines without any perturbations, such as drug treatments, gene knock-in/knock-down. Twelve classical markers used to characterize breast tumors were included to reveal the gene signatures across the intrinsic breast cancer subtypes. In addition, 19 EMT up- or down-regulated genes were selected to reveal the EMT features. Please see SI for the list of the sources of the gene expression data (SI Table S3) and the list of the selected genes (SI Table S4).

Immunofluorescence and structured illumination microscopy. Cells were grown on an 8-well chambered coverglass (154534, Thermo Scientific), fixed with 4% formaldehyde (F8775, Sigma-Aldrich), and permeabilized with 0.1% Triton X-100/PBS (Triton X-100, T8787, Sigma-Aldrich) prior blocking with 1% BSA in PBS. Then, the samples were incubated with antibodies overnight at 4 °C. To assess EMT status, cells were characterized by an EMT immunochemistry kit (SC026, R&D systems). The Alexa Fluor 633 Phalloidin (A22284, ThermoFisher Scientific) was used to stain actin filaments (F-actin). The fluorescence imaging was taken by Elyra S.1 Structured Illumination Super-Resolution Microscope (SR-SIM) with a 63x 1.2 N.A. water objective. Please see SI Method S7 for detailed information.

Statistical analysis. The unpaired two-sample t-tests were used to determine whether two sets of diffusivities (D) or linear sizes of compartments (L) were significantly different from each other of two groups. The F-test was used to check whether the two samples have the same variance, then according to the result of F-test, unpaired two-sample t-test with either equal variance or unequal variance was applied to test the null hypothesis: the means (D or L) of two populations are equal. Rather than a normal distribution, lognormal distribution was often used to describe the broad distribution of particle-trajectory-derived diffusivity[76,77]. The central limit theorem can be applied in the t-tests because of the great numbers of trajectories we collected in our study (at least 300 trajectories), and the t-test is valid even when D and L follow a lognormal distribution. The t-test is based on the two groups means $\overline{X_1}$ and $\overline{X_2}$. Because of the central limit theorem, the distribution of $\overline{X_1}$ and $\overline{X_2}$, in repeated sampling, converges to a normal distribution, irrespective of the distribution of X in the population[78]. Thus t-test is able to be used to test D and L among cell lines or cell lines with different treatments. In Figs 1–6, the error bar represents standard error of the mean $\left(\frac{Standard\ \ deviaiton}{\sqrt{size\ \ of\ \ the\ \ sample}}\right)$.

Many groups have shown that the transmembrane receptors exhibit complex dynamics[19,79,80].It is therefore common to fit the diffusivity histograms of the receptors with lognormal distribution and Gaussian mixture model[81]. Here we used the MATLAB built-in function, fitgmdist, to fit the histograms and evaluated the goodness of fit by the Akaike information criterion (AIC)[82,83]. The best-fitted number of components were decided by the fitting with the smallest AIC. From our previous study[19], three major populations were often seen in the EGFR diffusivity distribution. We evaluated the goodness of fit in one to three components, and presented the fitting results with the lowest AIC. The fitting means and standard deviations of log D were used to derive the arithmetic means and arithmetic standard deviations of D. Please see SI Method S8 for the derivation of these two arithmetic moments.

Homogeneous time-resolved fluorescence (HTRF) analysis. Quantification of phosphorylated EGFR levels was performed using the HTRF-Cellular kits: Phospho-EGFR (Tyr1068) Cellular Assay Kit (64EG1PEG, cisbio) and Total EGFR Cellular Assay Kit (64NG1PEG, cisbio). The specific EGFR phosphorylation on Tyr1068 and the total EGFR were measured after EGF-stimulation (20 ng/mL EGF (recombinant human epidermal growth factor, PHG0311L, Thermo Fisher Scientific) in serum-free DMEM/F12 medium). We followed the two-plate assay protocol provided by the vendor (SI Method S9 for a detailed description).

References

1. Blume-Jensen, P. & Hunter, T. Oncogenic kinase signalling. *Nature* **411**, 355–365 (2001).
2. Casaletto, J. B. & McClatchey, A. I. Spatial regulation of receptor tyrosine kinases in development and cancer. *Nature Reviews Cancer* **12**, 387–400 (2012).
3. Salaita, K. *et al*. Restriction of receptor movement alters cellular response: physical force sensing by EphA2. *Science* **327**, 1380–1385 (2010).
4. Kenny, P. A. *et al*. The morphologies of breast cancer cell lines in three-dimensional assays correlate with their profiles of gene expression. *Molecular Oncology* **1**, 84–96 (2007).
5. Calzado-Martín, A., Encinar, M., Tamayo, J., Calleja, M. & San Paulo, A. Effect of actin organization on the stiffness of living breast cancer cells revealed by peak-force modulation atomic force microscopy. *ACS Nano* **10**, 3365–3374 (2016).
6. Bao, G. & Suresh, S. Cell and molecular mechanics of biological materials. *Nature Materials* **2**, 715 (2003).
7. Kramer, N. *et al*. *In vitro* cell migration and invasion assays. *Mutation Research/Reviews in Mutation Research* **752**, 10–24 (2013).
8. Network TPS-OC. A physical sciences network characterization of non-tumorigenic and metastatic cells. *Scientific Reports* **3**, 1449 (2013).
9. Darling, E. M. & Di Carlo, D. High-throughput assessment of cellular mechanical properties. *Annual Review of Biomedical Engineering* **17**, 35–62 (2015).
10. Hochmuth, R. M. Micropipette aspiration of living cells. *Journal of Biomechanics* **33**, 15–22 (2000).
11. Dao, M., Lim, C. T. & Suresh, S. Mechanics of the human red blood cell deformed by optical tweezers. *Journal of the Mechanics and Physics of Solids* **51**, 2259–2280 (2003).
12. Gschwind, A., Fischer, O. M. & Ullrich, A. The discovery of receptor tyrosine kinases: targets for cancer therapy. *Nature Reviews Cancer* **4**, 361–370 (2004).
13. Den Hartigh, J. C., en Henegouwen, Pv. B., Verkleij, A. J. & Boonstra, J. The EGF receptor is an actinbinding protein. *The Journal of Cell Biology* **119**, 349–355 (1992).
14. Wiegant, F. *et al*. Epidermal growth factor receptors associated to cytoskeletal elements of epidermoid carcinoma (A431) cells. *The Journal of Cell Biology* **103**, 87–94 (1986).
15. Chung, I. *et al*. Spatial control of EGF receptor activation by reversible dimerization on living cells. *Nature* **464**, 783–787 (2010).
16. Low-Nam, S. T. *et al*. ErbB1 dimerization is promoted by domain co-confinement and stabilized by ligand binding. *Nature Structural & Molecular Biology* **18**, 1244–1249 (2011).
17. Saxton, M. J. & Jacobson, K. Single-particle tracking: applications to membrane dynamics. *Annual Review of Biophysics and Biomolecular Structure* **26**, 373–399 (1997).
18. Martin, D. S., Forstner, M. B. & Käs, J. A. Apparent subdiffusion inherent to single particle tracking. *Biophysical Journal* **83**, 2109–2117 (2002).
19. Liu, Y.-L. *et al*. Segmentation of 3D trajectories acquired by TSUNAMI microscope: an application to EGFR trafficking. *Biophysical Journal* **111**, 2214–2227 (2016).
20. Neve, R. M. *et al*. A collection of breast cancer cell lines for the study of functionally distinct cancer subtypes. *Cancer Cell* **10**, 515–527 (2006).
21. Prat, A. & Perou, C. M. Deconstructing the molecular portraits of breast cancer. *Molecular Oncology* **5**, 5–23 (2011).
22. Oberst, M. *et al*. Matriptase and HAI-1 are expressed by normal and malignant epithelial cells in vitro and in vivo. *The American Journal of Pathology* **158**, 1301–1311 (2001).
23. Prat, A. *et al*. Phenotypic and molecular characterization of the claudin-low intrinsic subtype of breast cancer. *Breast Cancer Research* **12**, R68 (2010).
24. Lim, E. *et al*. Aberrant luminal progenitors as the candidate target population for basal tumor development in BRCA1 mutation carriers. *Nature Medicine* **15**, 907 (2009).
25. Hruz, T. *et al*. Genevestigator v3: a reference expression database for the meta-analysis of transcriptomes. *Advances in Bioinformatics* **2008** (2008).
26. Taube, J. H. *et al*. Core epithelial-to-mesenchymal transition interactome gene-expression signature is associated with claudin-low and metaplastic breast cancer subtypes. *Proceedings of the National Academy of Sciences* **107**, 15449–15454 (2010).
27. Creighton, C. J. *et al*. Residual breast cancers after conventional therapy display mesenchymal as well as tumor-initiating features. *Proceedings of the National Academy of Sciences* **106**, 13820–13825 (2009).
28. Hennessy, B. T. *et al*. Characterization of a naturally occurring breast cancer subset enriched in epithelialto mesenchymal transition and stem cell characteristics. *Cancer Research* **69**, 4116–4124 (2009).
29. Thiery, J. P., Acloque, H., Huang, R. Y. & Nieto, M. A. Epithelial-mesenchymal transitions in development and disease. *Cell* **139**, 871–890 (2009).
30. De Rooij, J. Cadherin adhesion controlled by cortical actin dynamics. *Nature Cell Biology* **16**, 508–510 (2014).
31. Thiery, J. P. & Sleeman, J. P. Complex networks orchestrate epithelial–mesenchymal transitions. *Nature Reviews Molecular Cell Biology* **7**, 131–142 (2006).
32. Yilmaz, M. & Christofori, G. EMT, the cytoskeleton, and cancer cell invasion. *Cancer and Metastasis Reviews* **28**, 15–33 (2009).
33. Yilmaz, M. & Christofori, G. Mechanisms of motility in metastasizing cells. *Molecular Cancer Research* **8**, 629–642 (2010).
34. Ridley, A. J. Life at the leading edge. *Cell* **145**, 1012–1022 (2011).
35. Kusumi, A. *et al*. Paradigm shift of the plasma membrane concept from the two-dimensional continuum fluid to the partitioned fluid: high-speed single-molecule tracking of membrane molecules. *Annu. Rev. Biophys. Biomol. Struct.* **34**, 351–378 (2005).
36. Kusumi, A., Suzuki, K. G. N., Kasai, R. S., Ritchie, K. & Fujiwara, T. K. Hierarchical mesoscale domain organization of the plasma membrane. *Trends in Biochemical Sciences* **36**, 604–615 (2011).
37. Manzo, C. & Garcia-Parajo, M. F. A review of progress in single particle tracking: from methods to biophysical insights. *Reports on Progress in Physics* **78**, 124601 (2015).
38. Krapf, D. Mechanisms underlying anomalous diffusion in the plasma membrane. *Current Topics in Membranes* **75**, 167–207 (2015).
39. Kasai, R. S. & Kusumi, A. Single-molecule imaging revealed dynamic GPCR dimerization. *Current Opinion in Cell Biology* **27**, 78–86 (2014).
40. Almeida, P. F. F., Vaz, W. L. C. & Thompson, T. E. Lateral diffusion and percolation in 2-phase, 2-component lipid bilayers - topology of the solid-phase domains inplane and across the lipid bilayer. *Biochemistry* **31**, 7198–7210 (1992).
41. Zhu, J. X. *et al*. Decorin evokes protracted internalization and degradation of the epidermal growth factor receptor via caveolar endocytosis. *Journal of Biological Chemistry* **280**, 32468–32479 (2005).
42. Pinaud, F. *et al*. Dynamic Partitioning of a Glycosyl-Phosphatidylinositol-Anchored Protein in Glycosphingolipid-Rich Microdomains Imaged by Single-Quantum Dot Tracking. *Traffic* **10**, 691–712 (2009).
43. Weigel, A. V., Tamkun, M. M. & Krapf, D. Quantifying the dynamic interactions between a clathrin-coated pit and cargo molecules. *Proceedings of the National Academy of Sciences* **110**, E4591–E4600 (2013).
44. Lingwood, D. & Simons, K. Lipid rafts as a membrane-organizing principle. *Science* **327**, 46–50 (2010).
45. Saxton, M. J. Single-Particle Tracking - Effects of Corrals. *Biophysical Journal* **69**, 389–398 (1995).
46. Fujiwara, T., Ritchie, K., Murakoshi, H., Jacobson, K. & Kusumi, A. Phospholipids undergo hop diffusion in compartmentalized cell membrane. *Journal of Cell Biology* **157**, 1071–1082 (2002).

47. Andrews, N. L. *et al*. Actin restricts Fcϵ RI diffusion and facilitates antigen-induced receptor immobilization. *Nature Cell Biology* **10**, 955–963 (2008).
48. Wakatsuki, T., Schwab, B., Thompson, N. C. & Elson, E. L. Effects of cytochalasin D and latrunculin B on mechanical properties of cells. *Journal of Cell Science* **114**, 1025–1036 (2001).
49. Jaqaman, K. & Grinstein, S. Regulation from within: the cytoskeleton in transmembrane signaling. *Trends in Cell Biology* **22**, 515–526 (2012).
50. Pryor, MeghanM. *et al*. Dynamic transition states of ErbB1 phosphorylation predicted by spatial stochastic modeling. *Biophysical Journal* **105**, 1533–1543 (2013).
51. Ibach, J. *et al*. Single particle tracking reveals that EGFR signaling activity is amplified in clathrin-coated pits. *PloS one* **10**, e0143162 (2015).
52. Persson, F., Lindén, M., Unoson, C. & Elf, J. Extracting intracellular diffusive states and transition rates from single-molecule tracking data. *Nature Methods* **10**, 265–269 (2013).
53. Suresh, S. Biomechanics and biophysics of cancer cells. *Acta Mater* **55**, 3989–4014 (2007).
54. Kumar, S. & Weaver, V. M. Mechanics, malignancy, and metastasis: the force journey of a tumor cell. *Cancer and Metastasis Reviews* **28**, 113–127 (2009).
55. Swaminathan, V. *et al*. Mechanical stiffness grades metastatic potential in patient tumor cells and in cancer cell lines. *Cancer Research* **71**, 5075–5080 (2011).
56. Xu, L. *et al*. Optimization and evaluation of a novel size based circulating tumor cell isolation system. *PloS one* **10**, e0138032 (2015).
57. Katayama, Y. *et al*. Real-time nanomicroscopy via three-dimensional single-particle tracking. *Chemphyschem* **10**, 2458–2464 (2009).
58. Pavani, S. R. P. *et al*. Three-dimensional, single-molecule fluorescence imaging beyond the diffraction limit by using a double-helix point spread function. *Proceedings of the National Academy of Sciences* **106**, 2995–2999 (2009).
59. Wells, N. P. *et al*. Time-resolved three-dimensional molecular tracking in live cells. *Nano Letters* **10**, 4732–4737 (2010).
60. Ram, S., Kim, D., Ober, R. J. & Ward, E. S. 3D single molecule tracking with multifocal plane microscopy reveals rapid intercellular transferrin transport at epithelial cell barriers. *Biophysical Journal* **103**, 1594–1603 (2012).
61. Welsher, K. & Yang, H. Multi-resolution 3D visualization of the early stages of cellular uptake of peptidecoated nanoparticles. *Nature Nanotechnology* **9**, 198–203 (2014).
62. Suzuki, K. G. *et al*. Transient GPI-anchored protein homodimers are units for raft organization and function. *Nature Chemical Biology* **8**, 774–783 (2012).
63. Perillo, E. P. *et al*. Deep and high-resolution three-dimensional tracking of single particles using nonlinear and multiplexed illumination. *Nature Communications* **6**, 7874 (2015).
64. Howarth, M. *et al*. Monovalent, reduced-size quantum dots for imaging receptors on living cells. *Nature Methods* **5**, 397–399 (2008).
65. Ye, F. *et al*. Semiconducting polymer dots with monofunctional groups. *Chemical Communications* **50**, 5604–5607 (2014).
66. Hartman, Z., Zhao, H. & Agazie, Y. M. HER2 stabilizes EGFR and itself by altering autophosphorylation patterns in a manner that overcomes regulatory mechanisms and promotes proliferative and transformation signaling. *Oncogene* **32**, 4169 (2013).
67. Alroy, I. & Yarden, Y. The ErbB signaling network in embryogenesis and oncogenesis: signal diversification through combinatorial ligand-receptor interactions. *FEBS Letters* **410**, 83–86 (1997).
68. DeFazio-Eli, L. *et al*. Quantitative assays for the measurement of HER1-HER2 heterodimerization and phosphorylation in cell lines and breast tumors: applications for diagnostics and targeted drug mechanism of action. *Breast Cancer Research* **13**, R44 (2011).
69. Debnath, J., Muthuswamy, S. K. & Brugge, J. S. Morphogenesis and oncogenesis of MCF-10A mammary epithelial acini grown in three-dimensional basement membrane cultures. *Methods* **30**, 256–268 (2003).
70. Kusumi, A., Tsunoyama, T. A., Hirosawa, K. M., Kasai, R. S. & Fujiwara, T. K. Tracking single molecules at work in living cells. *Nature Chemical Biology* **10**, 524–532 (2014).
71. Jaumouillé, V. *et al*. Actin cytoskeleton reorganization by Syk regulates Fcγ receptor responsiveness by increasing its lateral mobility and clustering. *Developmental Cell* **29**, 534–546 (2014).
72. Freeman, S. A. *et al*. Toll-like receptor ligands sensitize B-cell receptor signalling by reducing actindependent spatial confinement of the receptor. *Nature Communications* **6**, 6168 (2015).
73. Freeman, S. A. *et al*. Transmembrane pickets connect cyto-and pericellular skeletons forming barriers to receptor engagement. *Cell* **172**, 305–317.e310 (2018).
74. Scheel, C. *et al*. Paracrine and autocrine signals induce and maintain mesenchymal and stem cell states in the breast. *Cell* **145**, 926–940 (2011).
75. Dahan, M. *et al*. Diffusion dynamics of glycine receptors revealed by single-quantum dot tracking. *Science* **302**, 442–445 (2003).
76. Wade, W. F., Freed, J. H. & Edidin, M. Translational diffusion of class II major histocompatibility complex molecules is constrained by their cytoplasmic domains. *The Journal of Cell Biology* **109**, 3325–3331 (1989).
77. Saxton, M. J. Single-particle tracking: the distribution of diffusion coefficients. *Biophysical Journal* **72**, 1744 (1997).
78. Casella, G. & Berger, R. L. *Statistical inference*. Vol. 2 (Duxbury Pacific Grove, CA, 2002).
79. Clausen, M. P. & Lagerholm, B. C. Visualization of plasma membrane compartmentalization by high-speed quantum dot tracking. *Nano Letters* **13**, 2332–2337 (2013).
80. Montiel, D., Cang, H. & Yang, H. Quantitative characterization of changes in dynamical behavior for singleparticle tracking studies. *The Journal of Physical Chemistry B* **110**, 19763–19770 (2006).
81. Knight, S. C. *et al*. Dynamics of CRISPR-Cas9 genome interrogation in living cells. *Science* **350**, 823–826 (2015).
82. Sclove, S. L. Application of model-selection criteria to some problems in multivariate analysis. *Psychometrika* **52**, 333–343 (1987).
83. Celeux, G. & Soromenho, G. An entropy criterion for assessing the number of clusters in a mixture model. *Journal of Classification* **13**, 195–212 (1996).

Acknowledgements

We thank Dr. Amy Brock for providing us with the MCF10A, MCF7, and MDA-MB-231 cell lines, and Dr. Keith Lidke for sharing the 2D-SPT software with us. This work was supported by Robert A. Welch Foundation (F-1833), the Texas 4000, NIH grants CA193038 (to H.-C. Yeh) and CA211615 (to M.-C. Hung), CPRIT grants DP150052 (to M.-C. Hung) and RR160005 (to T. E. Yankeelov), Breast Cancer Research Foundation (BCRF-17-069 to M.-C. Hung), and National Breast Cancer Foundation, Inc.

Author Contributions

Y.-L. Liu, C.-K. Chou, and H.-C. Yeh conceived the project and wrote the article. Y.-L. Liu, M. Kim, R. Vasisht, Y.-A. Kuo, K. Blocher, H. Horng, Y.-I. Chen, and D.T. Nguyen performed cell culture, prepared samples, and conducted tracking experiments. Y.-L. Liu, C. Liu and E. P. Perillo developed the trajectory analysis algorithm. Y.-A. Chen advised the gene expression analysis. M. Kim, P. Ang conducted the gene expression analysis. M. Kim, R. Vasisht and Y.-A. Kuo conducted image processing. Y.-L. Liu and C.-K. Chou analyzed the results. T.E. Yankeelov, A.K. Dunn and M.-C. Hung helped interpret the tracking results. H.-C. Yeh supervised the project.

Additional Information

Supplementary information accompanies this paper at https://doi.org/10.1038/s41598-018-37625-0.

Competing Interests: The authors declare no competing interests.

Supplementary Information

Assessing metastatic potential of breast cancer cells based on EGFR dynamics

Yen-Liang Liu[1], Chao-Kai Chou[2], Mirae Kim[1], Rohan Vasisht[1], Yu-An Kuo[1], Phyllis Ang[3], Cong Liu[1], Evan P. Perillo[1], Yu-An Chen[1], Katherine Blocher[1], Hannah Horng[4], Yuan-I Chen[1], Duc Trung Nguyen[1], Thomas E. Yankeelov[1,5,6,7,8], Mien-Chie Hung[2,9], Andrew K. Dunn[1], & Hsin-Chih Yeh*[,1]

[1]Department of Biomedical Engineering, The University of Texas at Austin, Austin, TX, USA

[2]Department of Molecular and Cellular Oncology, The University of Texas MD Anderson Cancer Center, Houston, TX, USA

[3]Department of Electrical and Computer Engineering, The University of Texas at Austin, Austin, TX, USA

[4]Department of Bioengineering, The University of Maryland, College Park, MD, USA

[5]Institute for Computational Engineering and Sciences, The University of Texas, Austin, TX, USA

[6]Department of Diagnostic Medicine, Dell Medical School, The University of Texas at Austin, Austin, TX, USA

[7]Department of Oncology, Dell Medical School, The University of Texas at Austin, Austin, TX, USA

[8]Livestrong Cancer Institutes, The University of Texas at Austin, Austin, Texas, USA

[9]Center for Molecular Medicine and Graduate Institute of Cancer Biology, China Medical University, Taichung, Taiwan

[10]Texas Materials Institute, The University of Texas at Austin, Austin, TX, USA

Content

Method S1 | Cell culture 2
Method S2 | Fluorescent probe labeling to EGFR 2
Method S3 | Data processing 2
Method S4 | Single Particle Tracking 3
Method S5 | Extracting dynamic parameters from MSD 3
Method S6 | Calculation of luminal differentiation score 4
Method S7 | Immunofluorescence and structured illumination microscopy 4
Method S8 | Derivation of arithmetic moments from normally distributed log *D* and log *L* 5
Method S9 | Homogenous time-resolved fluorescence (HTRF) 5
Figure S1 | Assays for biophysical characterization of cells 7
Figure S2 | LatB changes the diffusivity of EGFR and the size of microdomains. 8
Figure S3 | Cassette compatibility of TReD assay 9
Figure S4 | Correlations between EGFR diffusivity and expression levels of EGFR family 10
Table S1 | Molecular classification, clinical and pathological features, and sources of cell lines 11
Table S2 | Source of gene expression data (mRNA microarray) 12
Table S3 | Selected genes for gene expression analysis 13
Supplementary References 14

Method S1 | Cell culture

BT474, SKBR3, MDA-MB-468, MDA-MB-231, BT549 were grown in DMEM/F12 medium (11320082, Thermo Fisher Scientific) supplemented with 10% fetal bovine serum (16140071, Thermo Fisher Scientific) and 50 U/mL penicillin-streptomycin (15070063, Thermo Fisher Scientific). MCF7 was grown in MEM (11095-080, Thermo Fisher Scientific) supplemented with 10% fetal bovine serum and 50 U/mL penicillin-streptomycin. The benign breast epithelial cell line, MCF10A, was maintained as described [1]. The recipe of MCF10A medium is DMEM/F12 medium supplemented with 5% horse serum (16050122, Thermo Fisher Scientific), 20 ng/mL epidermal growth factor (AF-100-15, Peprotech), 0.5 μg/mL hydrocortisone (H0888, Sigma-Aldrich), 100 ng/mL cholera toxin (C8052, Sigma-Aldrich), 10 μg/mL insulin (I9278, Sigma-Aldrich), and 50 U/mL penicillin-streptomycin. These cells were kept in a humidified atmosphere with 5% CO2 in air at 37ºC. Single suspensions were prepared by mild enzymatic dissociation using a 0.25% trypsin/EDTA solution (25200-056, Thermo Fisher Scientific). For immunofluorescence and SPT experiments, cells were grown on an optical imaging 8-well chambered coverglass (154534, Thermo Scientific).

Method S2 | Fluorescent probe labeling to EGFR

Anti-EGFR IgG antibody-conjugated fluorescent nanoparticles (FN-IgG) were used to label EGFR for tracking. Biotinylated monoclonal anti-EGFR antibodies (Clone Ab-3, MS-311-B, Thermo Fisher Scientific) were mixed at 1:1 ratio with ⌀40 nm NeutrAvidin-labeled red fluorescent nanoparticles (F8770, Thermo Fisher Scientific) in 1.5% bovine serum albumin (BSA, S7806, Sigma-Aldrich) in PBS solution. The Ab-3 does not interfere with the binding of EGF to EGFR. The FN-IgG (30 nM for the stock solution) can be stored at 4ºC for up to 1 week. The number of antibodies per nanoparticle should follow a Poisson distribution[2]. For EGFR tracking, cells were seeded onto optical imaging 8-well chambered coverglass (154534, Thermo Fisher Scientific) with a cell density of 1×10^5 cells per well and allowed to grow to 70-80% cell confluency. Before tracking experiments, cells were stained with Hoechst 33258 (H3569, Thermo Fisher Scientific, 1:1000 dilution in cell culture medium) for 10 minutes at 37ºC. Then, the staining buffer was replaced with the EGFR-labeling solution (FN-IgG at 100 pM) diluted from the stock solution (30 nM). The reaction was incubated for 10 minutes at 37ºC. The EGFR-labeling solution was removed, and the samples were washed twice using PBS to remove the unbound fluorescent nanoparticles. The volumes of all solutions and washing buffers used in staining were 200 µl per well. Upon completion of nucleus staining and EGFR labeling, the chambered coverglass was immediately put on the microscope for tracking experiments. All imaging was conducted at 37 °C using a temperature-controlled stage (Stable Z System, Bioptechs).

Method S3 | Data processing

All data analysis and image processing were performed within the MATLAB (The Mathworks Inc.) environment, including the DIPImage[3] image processing library. The images were taken with HCImage (a Hamamatsu's image acquisition and analysis software), and the single particle trajectories were reconstructed by using a single-particle tracking software developed by Lidke's group[4]. Later, the trajectories were processed into mean-squared displacement curves where the diffusion coefficient (D) and the linear dimension of the compartment (L) were extracted by curve fitting (**Method S5**, also see our previous publication[5] for a detailed description).

Method S4 | Single Particle Tracking

Single particle trajectories were determined from the raw data sets using a three-step process: (i) Identifying contiguous regions of pixels; (ii) Gaussian fitting; (iii) building trajectories from coordinates. This approach is similar to those described previously[4, 6, 7].

1. Identifying continugous regions of pixels. A series of 2D images in time trace was processed independently to find FN-IgG-EGFR coordinates. The contiguous regions of pixels, which represent the images of fluorescent particles, were identified on the basis of two criteria: (i) pixels had intensities greater than 3-fold the standard deviation of pixel intensities from areas defined as background (background offset algorithm[3]) and (ii) pixels were above a threshold[3]. Then, a high pass filtering was applied to the image with a 2D Gaussian filter ($\sigma = 5$). The binary image of pixels passing both criteria was later processed by Gaussian fitting.

2. Gaussian fitting. To find out the center of the fluorescent particles, the center of mass of each contiguous region in the binary image was set as the starting point in a Gaussian fitting routine. The highest intensity pixel in a small region around the starting point (5 pixels square) was used as an updated starting. Fits were performed in a square region, of size ~ $2^*\sigma_{xy}$, around the updated starting point. The σ_{xy} defines the size of 2D Gaussian approximation to the point spread function. After convergence of the fitting routine (a change in location of fewer than 10^{-5} pixels), a normalized cross-correlation was calculated to verify the 2D Gaussian-fitted coordinates. The found coordinates were only considered as positions of FN-IgG-EGFR and used in the further analysis if they exceeded a cross-correlation value of 0.7.

3. Building trajectories from coordinates. The probability of finding a diffusing particle with diffusivity *D* in two dimensions at a distance greater than *d* from its starting point after a time Δt is given by[8]

$$P(d, \Delta t) = exp\left[\frac{-d^2}{4D\Delta t}\right] \qquad (1)$$

Trajectories were built from the set of 3D coordinates (x,y, and t) in two steps. First, coordinates identified at time *t* were compared with coordinates at time $t+\Delta t$ using Eq. 1 where Δt is the inverse frame rate of data acquisition. If $P(r, \Delta t)$ was found to be greater than .05, the coordinate at $t+\Delta t$ is associated with the coordinate at *t* in a trajectory. This process builds short, un-interrupted trajectories. Second, to connect these short trajectories originated from the same targets, the end coordinate of all trajectories was compared with all later starting coordinates of other trajectories using Eq. 1, where Δt is now the time interval between the end of the first trajectory and the beginning of the second. The later trajectory with the smallest Δt that has a $P(r, \Delta t) > 0.01$ is connected with the first trajectory. This process is continued until there are no remaining pairs of trajectories that satisfy the criteria. The reconstructed trajectories are further processed into mean-squared displacement to estimate diffusion coefficient.

Method S5 | Extracting dynamic parameters from MSD

The typical approach to analyze a single-particle trajectory starts with the calculation of mean-squared displacement (MSD)[9, 10], which describes the average squared distance (d^2, *r* is the position vector) that the particle has explored in space at a given time lag (Δt):

$$MSD(\Delta t) = \langle (\boldsymbol{r}(t + \Delta t) - \boldsymbol{r}(t))^2 \rangle \qquad (2)$$

Similar to many groups[11, 12], we have observed that EGFR movement exhibited hop diffusion on the plasma membrane[5]. The dynamics parameters, the diffusivity (*D*) and the linear dimension of compartments (*L*), are extracted from trajectories by fitting the MSD curves. The *D* was defined as the linear MSD fitting result of the first 5 MSD points, and in the short time domain, the EGFR movement would act like Brownian motion:

$$MSD(\Delta t) = \langle(\boldsymbol{r}(t+\Delta t) - \boldsymbol{r}(t))^2\rangle = 4D_{1-5}\Delta t + \sigma_{xy}^2 \qquad (3)$$

The offset, σ_{xy}^2, specifies the localization precision σ_{xy} which was estimated using trajectories of fixed nanoparticles. The localization precision of our system is 7.3 ± 3.0 nm (mean ± standard deviation). For *L*, the MSD curves were fitted with an equation for confined diffusion[13, 14], and *L* was defined as the MSD fitting result of the first 10 MSD points :

$$MSD(\Delta t) \cong \frac{L^2}{3}\left[1 - \exp\left(-\frac{\Delta t}{\tau}\right)\right] + 4D_{macro}\Delta t + \sigma_{xy}^2 \qquad (4)$$

Confined diffusion is featured by an abrupt change of slope in the MSD curve[11] after a characteristic equilibration time *τ*. In **Figure 1D**, the averaged MSD curves are down-ward curves within 0.5 second time window, which indicates the EGFRs exhibited confined diffusion. Therefore, we are able to extract the linear dimension of compartments (*L*).

Method S6 | Calculation of luminal differentiation score

The luminal differentiation predictor was developed by Perou group[15] and trained with the database GSE16997 which is contributed by Partanen group[16]. Then this predictor was applied to the UNC337 database (GSE18229 in GEO) to calculate the luminal differentiation scores of 39 tumor samples (n = 337). According to the molecular characterization, these 39 tumor samples have been classified into the 5 subtypes of breast cancer: Luminal A, Luminal B, HER2-enriched, Basal, and Claudin-low. Using gene expression profiling, Partanen group identified three epithelial cell-enriched subpopulations in the GSE16997 database: mammary stem cells (MaSC), luminal progenitors (pL) and mature luminal cells (mL). On the basis of the gene expression pattern of GSE16997 and these three classified subpopulations, the luminal differentiation predictor uses Distance-Weighted Discrimination (DWD)[17], a type of High Dimension Low Sample Size statistical analysis methods, to define the separating hyperplane (with greatest variation between classified groups) and project the vectors of gene expression levels of tumor samples to the differentiation axes: MaSC⟶pL and pL⟶mL. In the training dataset (GSE16997), the pL centroid was set as the origin, and the MaSC and mL centroid were transformed to length 1 (sum of squares equals 1). After completing the differentiation model, each sample from UNC337 was then projected to the MaSC⟶pL axis and the pL⟶mL axis by calculating the inner product of the sample vector and the MaSC⟶pL vector or the pL⟶mL vector that was identified by DWD. The difference of the two projected positions of each sample along the MaSC⟶ pL⟶mL axis is defined as the differentiation score.

Method S7 | Immunofluorescence and structured illumination microscopy

Cells were grown on an optical imaging 8-well chambered coverglass (154534, Thermo Scientific), fixed with 4% formaldehyde (F8775, Sigma-Aldrich), and permeabilized with 0.1% Triton X-100/PBS (Triton X-100, T8787, Sigma-Aldrich) prior to blocking with 1% BSA in PBS. Then, the samples were incubated with antibodies overnight at 4ºC. To assess EMT status, cells were characterized with an EMT immunochemistry kit (SC026, R&D systems) which contains three types of fluorophore-tagged IgGs: NL557-conjugated goat anti-human snail, NL637-conjugated goat anti-human E-cadherin, and NL493-conjugated goat anti-human vimentin. Cell nuclei were visualized with Hoechst 33258 (H3569, Thermo Fisher Scientific). The Alexa Fluor^{TM} 633 Phalloidin (A22284, ThermoFisher Scientific) was used to stain actin filaments (F-actin). The fluorescence imaging was taken by Elyra S.1 Structured Illumination Super-Resolution Microscope (SR-SIM) with a 63x 1.2 N.A. water objective. The SR-SIM system is equipped with 4 excitation laser wavelengths for standard fluorophores (405 nm, 488nm, 561 nm, and 633nm) and comes with emission filters for DAPI, GFP, RFP and Alexa 633.

Method S8 | Derivation of arithmetic moments from normally distributed log *D* and log *L*

The arithmetic mean ($\bar{X}$) and arithmetic standard deviation ($\sigma_{\bar{x}}$) shown in Figure 4 and Figure S2 were derived as follows. Given a log-normally distributed random variable X and two parameters μ and σ, which are, respectively, the mean and standard deviation of the variable's logarithm, then the logarithm of X is normally distributed, and we can write X as

$$X = 10^{\mu+\sigma Z} \tag{5}$$

with Z a standard normal variable[18]. Then the arithmetic mean and arithmetic standard deviation of the log-normally distributed X are given by[18]

$$\bar{X} = E[X] = 10^{\mu+0.5\sigma^2} \tag{6}$$

$$E[X^2] = 10^{2\mu+2\sigma^2} \tag{7}$$

$$Var[X] = E[X^2] - \left[E[X]\right]^2 = 10^{2\mu+\sigma^2}(10^{\sigma^2} - 1) \tag{8}$$

$$\sigma_{\bar{x}} = SD[X] = \sqrt{Var[X]} = E[X]\sqrt{10^{\sigma^2} - 1} = 10^{\mu+0.5\sigma^2}\sqrt{10^{\sigma^2} - 1} \tag{9}$$

Method S9 | Homogenous time-resolved fluorescence (HTRF)

Cells were seeded in 96-well culture plates with the seeding density of 20,000 cells/well. After 2-day incubation followed 1-day serum starvation, the cells were stimulated with 20 ng/mL EGF (recombinant human epidermal growth factor, PHG0311L, Thermo Fisher Scientific) in serum-free DMEM/F12 medium and subsequently lysed at a series of time points (0, 15, 30, 60, 120, 300 seconds). For EMT-induced cells, the cells were treated with the EMT-induction supplement for 3 days before being transferred in 96-well culture plates. The EMT-induced cells were incubated in the medium containing the EMT-induction supplement for 2-day and then 1-day starvation. The cellular lysates were transferred to two assay plates for Phospho-EGFR (Tyr1068) Cellular Assay Kit (64EG1PEG, cisbio) and Total EGFR Cellular Assay Kit (64NG1PEG, cisbio). Anti-phospho-EGFR-d2 (2µl) and anti-EGFR-Eu^{3+}-Cryptate (2µl) were added to each well and plates were incubated in the dark for 4h at room temperature. The HTRF signals were read by Flexstation® 3 of Molecular Devices, and the measurement conditions were listed below: 50 µs integration delay, 400 µs integration, 100 reading, 314 nm wavelength for both excitation 1 and 2, 665 nm for emission 1, 630 nm for cut off of emission 1, 620 nm for emission 2, and 570 nm for cut off of emission 2. The HTRF ratio, background corrected HTRF ratio, and the normalized value was calculated as

$$\text{HTRF Ratio} = \frac{Signal\ 665\ nm}{Signal\ 620\ nm} \times 10^4 \tag{10}$$

$$\begin{aligned}\Delta\text{R} &= \text{Background corrected HTRF Ratio} \\ &= HTRF\ Ratio_{sample} - HTRF\ Ratio_{background}\end{aligned} \tag{11}$$

$$\text{Normalized } \Delta\text{R} = \frac{\Delta R_{Phospho-EGFR}}{\Delta R_{Total-EGFR}} \times 100 \tag{12}$$

Levels of phosphorylated EGFR at different time points were further normalized to those obtained at 0s for each experimental group. Each data point has four repeats, and we have conducted three trials.

Schematic illustrations	Technique	Physical properties	Through-put	Cassette Compati-bility	Ref.
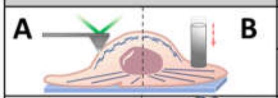	A. Atomic force microscopy	Viscoelasticity	Low	No	(19-21)
	B. Cytoindentation	Viscoelasticity	Low	No	(22)
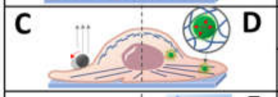	C. Magnetic twisting cytometry	Viscoelasticity	Low	No	(23,24)
	D. Particle-tracking microrheology	Viscoelasticity	Medium	No	(25-27)
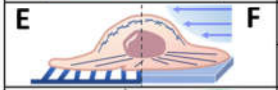	E. Microfabricated post array	Endogenous force	Medium	No	(28,29)
	F. Shear flow	Shear resistance	Medium	No	(30)
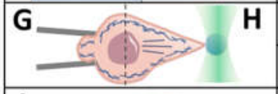	G. Micropipette aspiration	Elasticity and deformability	Low	No	(31)
	H. Optical tweezers	Membrane elasticity	Low	Yes	(32,33)
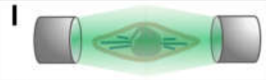	I. Optical stretcher	Whole-cell deformability	High	Yes	(34)
	J. Microfluidic assay	Whole-cell deformability	High	No	(35,36)
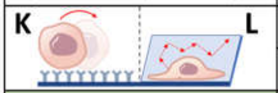	K. Cell rolling	Cell adhesion	Medium	No	(37)
	L. Cell migration	Cell motility	Medium	No	(38)
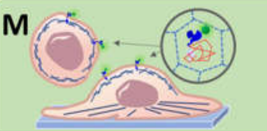	**M. Transmembrane Receptor Dynamics (TReD)**	1. Diffusivity 2. Microdomain size 3. Endocytosis speed 4. Active transport speed	Medium to high	Yes	

Figure S1 | Assays for biophysical characterization of cells

Fig. S1 summarized a variety of techniques for conducting physical or mechanical phenotyping of cells in term of principles, physical properties to be measured, throughput, and the cassette compatibility. AFM-based methods[19, 20, 21], cytoindentation[22], and magnetic twisting cytometry[23, 24] exert forces on a local region of an adherent cell. Therefore, these techniques suffer from low throughput, and the direct contact of probes with the cell surface may cause cellular responses. Without applied forces does particle-tracking microrheology[25, 26, 27] allow the measurement of intracellular viscoelasticity, but the ballistic injection or micro-injection of nanoparticles into cells requires significant time and might jeopardize cell viability. Cell traction force[28, 29] and shear stress resistance[30] which measured by microfabricated post array and shear flow technique, respectively, could also provide a better understanding of cancer cell metastasis. However, these six techniques we discussed above can be used only for cells adhered on a substrate, which would constrain the throughput and might limit their applicability of being integrated into BioMEMS-based circulating tumor cell (CTC) capture devices. Micropipette aspiration[31] has modest throughput and can deal with suspended cells, but it also can't avoid cell-tool interactions. Light-based cell-manipulation approaches, including optical tweezers[32, 33] and optical stretcher[34], are attractive methods that do not require mechanical contact with the cells under examination. However, one the limitations of using optical tweezers and optical stretcher for measuring the whole-cell deformability is the relatively small-magnitude force (10^{-9}-10^{-14} N) that can be applied. The force is not strong enough to deform most cell types sufficiently to obtain information about whole-cell properties. Microfluidic assays[35, 36], such as deformation passage and hydrodynamic stretching, provide high-throughput mechanical phenotyping of whole cells under precisely controlled fluid flow. The microfluidic channels need to be properly designed to avoid the induced mechanical stress on cells. The cell rolling[37] and the cell migration[38], only provide medium throughput. Our technique is an innovative approach to measure the physical properties of cells by tracking fluorescence-tagged transmembrane receptors. This technique can be easily integrated with a microfluidic CTC capture device which exhibits the high-throughput isolation of CTCs from blood (**Fig. S3**); this technique can deal with suspended cells and does not require mechanical contact or applied force with cells under examination. In addition, the acquired trajectories from several subcellular regions in one single cell (5-20 trajectories) would provide the higher spatial resolution than those from whole-cell measurements.

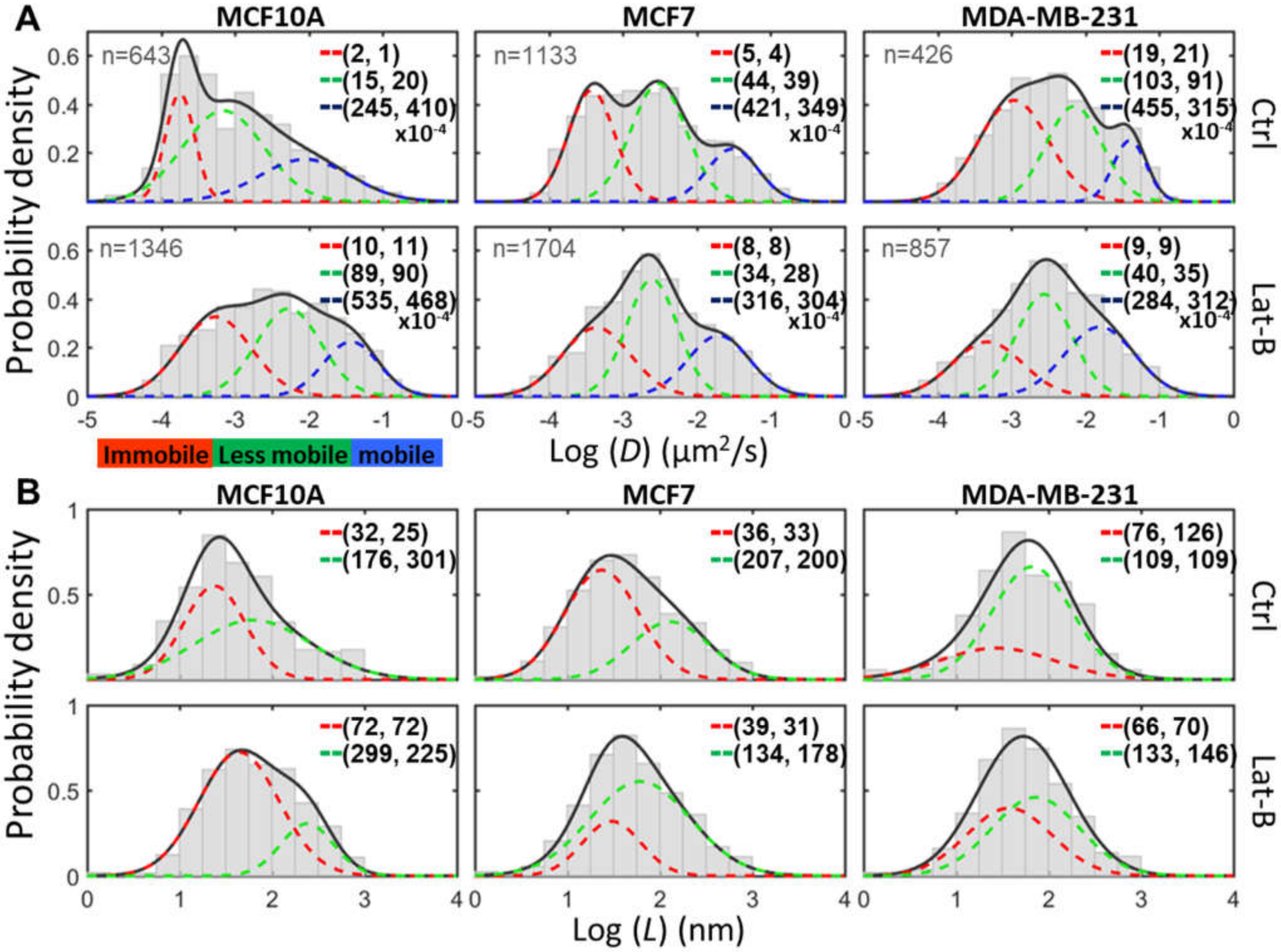

Figure S2 | LatB changes the diffusivity of EGFR and the size of microdomains.

Histograms of log D (**A**) and log L (**B**) extracted from FN-IgG-EGFRs trajectories in the three breast cell lines that were treated with/without 200 nM latrunculin B (LatB). The values shown in the histograms represent the arithmetic moments of D or L ((arithmetic means ($\bar{X}$) , arithmetic standard deviations($\sigma_{\bar{x}}$))) derived from Gaussian mixture model fitting of log D and log L (3 or 2 sub-populations). The three populations are defined as immobilization (red), less mobile (green), and mobile (blue). The number of trajectories from each group is labeled in (A).

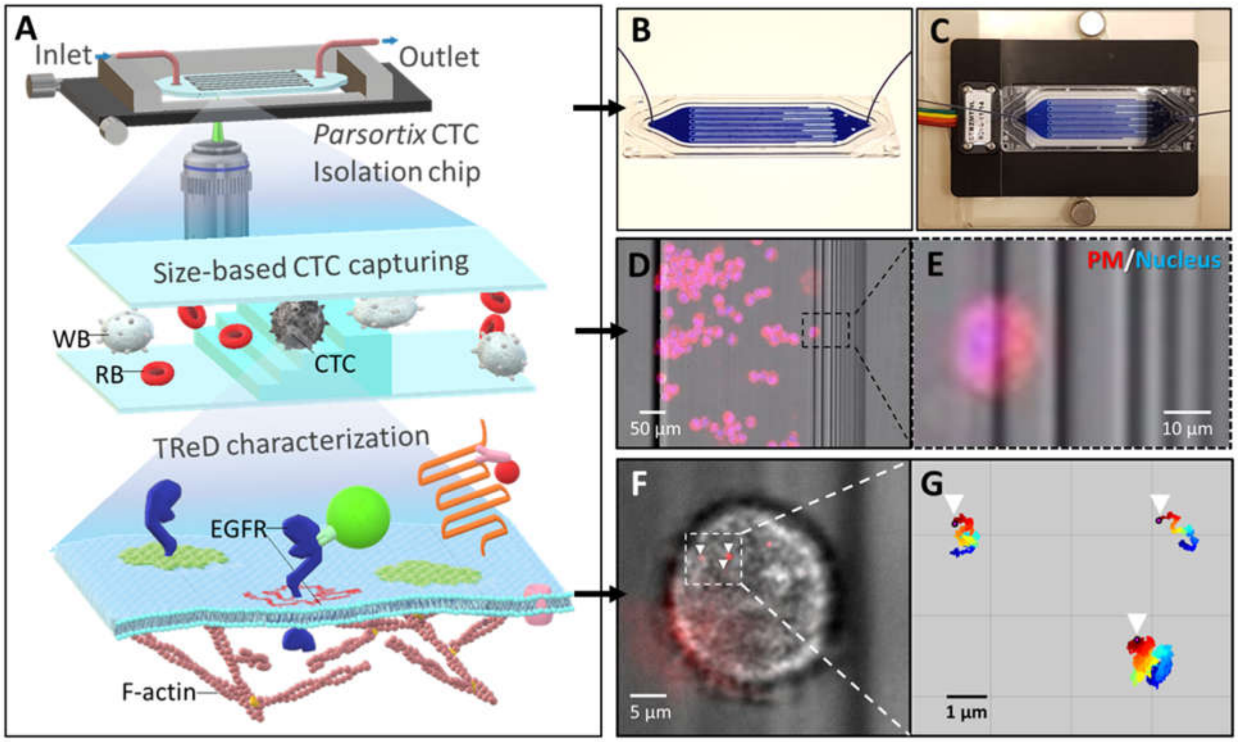

Figure S3 | Cassette compatibility of TReD assay

(A) The schematic shows the procedure of TReD assay applied in a cell-capturing microfluidic chip. We demonstrated the cassette compatibility on the Parsortix CTC isolation chip which uses the size-based cell capture technique to isolate cancer cells. Being trapped in the microfluidic chip, cells were tagged with FN-IgG and followed with SPT of FN-IgG-EGFR. (**B**) The Parsotix CTC isolation chip filled with blue ink. (**C**) The chip can be mounted on the temperature-controlled stage during tracking. (**D**) We use MDA-MB-231 as the substitute of CTCs to test the cassette compatibility of the TReD assay. The plasma membrane (PM) and nuclei were stained with CellMask-Deep Red and Hoechst, respectively. (**E**) The zoom-in shows a captured cell. **(F)** The EGFRs were tagged with FN-IgGs (red-colored and pointed by arrowheads) (**G**) The zoom-in shows the collected trajectories from a captured cell.

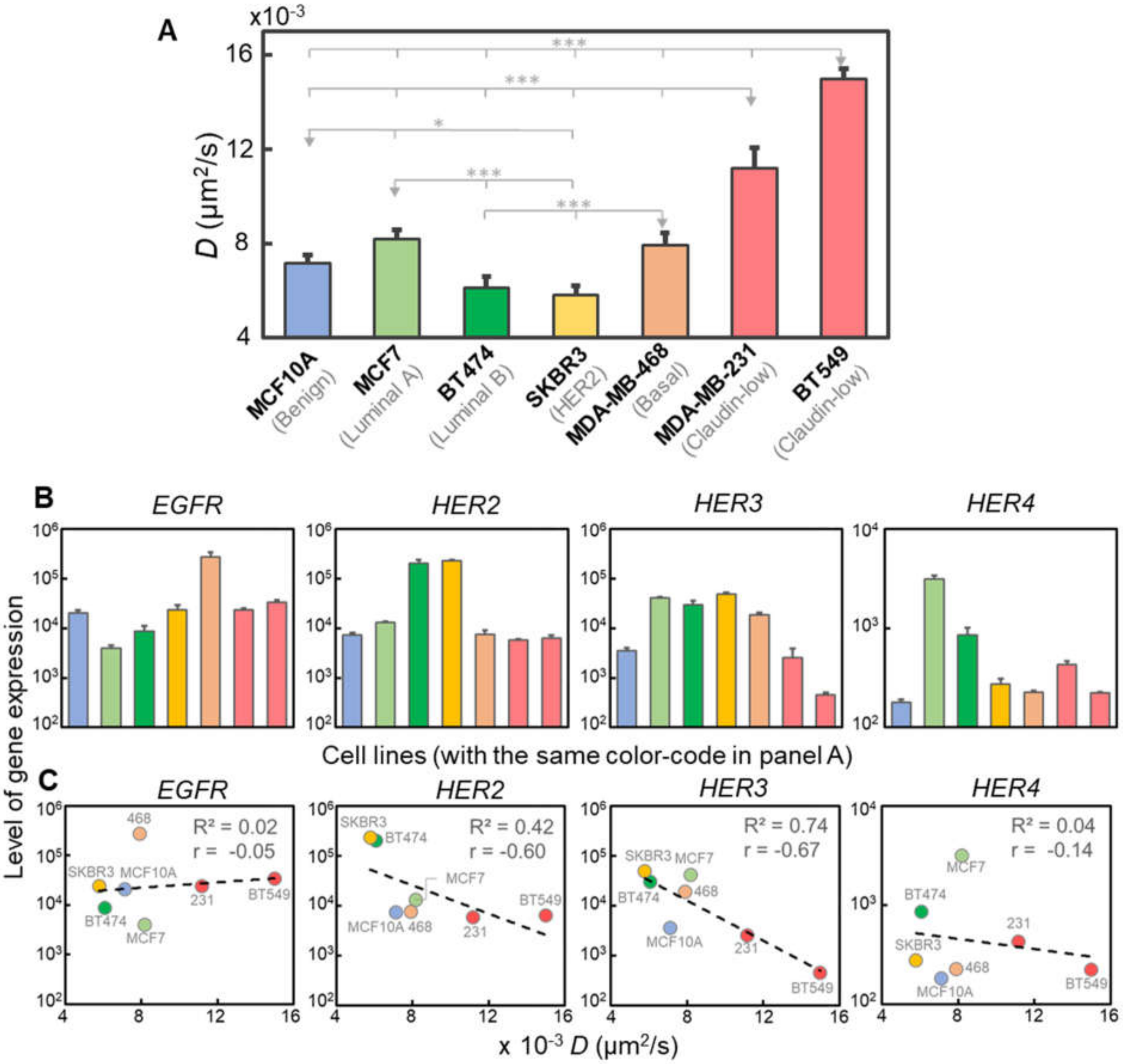

Figure S4 | Correlations between EGFR diffusivity and expression levels of EGFR family

(A) The diffusivity of EGFR complexes measured in these seven breast cell lines. The error bar represents the standard error. (**B**) mRNA expression levels of the EGFR family including *EGFR*, *HER2*, *HER3*, and *HER4* among these cells lines. Each bar is color-coded with the same color corresponding to each type of cells shown in panel A. (**C**) Correlations between expression levels of receptors to EGFR diffusivity. The R-squared is calculated by exponential curve fitting, and the r represents the correlation coefficient.

Table S1 | Molecular classification, clinical and pathological features, and sources of cell lines

Cell line	Subtype[#]	ER[ǂ]	PR[ǂ]	HER2[ǂ]	EGFR[ǂ]	*In vitro* invasiveness[†]	Source*	Tumor type*
MCF10A	**Benign**	**-**	**-**	**-**	**+**	**NA**	**Reduction mammoplasty**	**Fibrocystic disease**
MCF7	**Luminal A**	**+**	**+**	**-**	**-/+**	**+**	**Pleural effusion**	**Metastatic adenocarcinoma**
BT474	**Luminal B**	**-/+**	**+**	**+**	**+**	**+**	**Primary tumor**	**Invasive ductal carcinoma**
SKBR3	**HER2 -enriched**	**-**	**-**	**+**	**+**	**+**	**Pleural effusion**	**Adenocarcinoma**
MDA-MB-468	**Basal**	**-**	**-**	**-**	**+**	**+**	**Pleural effusion**	**Metastatic adenocarcinoma**
MDA-MB-231	**Claudin-low**	**-**	**-**	**-**	**+**	**+++**	**Pleural effusion**	**Metastatic adenocarcinoma**
BT549	**Claudin-low**	**-**	**-**	**-**	**+**	**+++**	**Primary tumor**	**Invasive ductal carcinoma**

Abbreviations: ER, estrogen receptor; PR, progesterone receptor; HER2, human epidermal growth factor receptor 2; EGFR, epidermal growth factor receptor.

[#] The five subtypes are determined from Neve's[39] and Prat's[40] study.

ǂ The biomolecular characteristics are determined from Neve's[39], Kao's[41], and Subik's[42] study.

[†] The levels of *in vitro* invasiveness are determined from Oberst's study[43].

*The information of source and tumor type is from the ATCC (https://www.atcc.org/)

Table S2 | Source of gene expression data (mRNA microarray)

Cell line	Source of gene expression data
MCF10A	GSE5823[44], GSE10070[45], GSE34211[46], E-MEXP-3682[47], E-MEXP-3407[48]
MCF7	GSE5823[44], GSE6521, GSE8597[49], GSE10879, GSE11135[50], GSE11324[51], GSE11352[52], GSE11506[53], GSE11791[54], GSE13477[55], GSE19123[56], GSE36133[57], GSE34211[46], E-MTAB-37[58], GSE46924[59], GSE57083, GSE32474[60], GSE31912[61], GSE36847[62], GSE29884
BT474	GSE5823[44], GSE36133[57], GSE34211[46], E-MTAB-37[58], GSE57083
SKBR3	GSE7562[63], GSE36133[57], GSE34211[46], GSE57083
MDA-MB-468	GSE36133[57], GSE57083
MDA-MB-231	GSE5823[44], GSE7307, GSE20089[64], GSE36133[57], GSE34211[46], GSE15893[65], GSE57083, GSE32474[60]
BT549	GSE36133[57], GSE34211[46], GSE57083, GSE32474[60]

Table S3 | Selected genes for gene expression analysis

Biomarkers for	Gene name	Protein name
Basal cell	*KRT5*	keratin 5
	KRT14	keratin 14
	KRT17	keratin 17
Luminal cell	*ERBB2*	erb-b2 receptor tyrosine kinase 2
	ESR1	estrogen receptor 1
	GATA3	GATA binding protein 3
	KRT18	keratin 18
	KRT19	keratin 19
	PGR	progesterone receptor
Claudin-low	*CLDN3*	claudin 3
	CLDN4	claudin 4
	CLDN7	claudin 7
EMT-up -regulated	*CDH2*	cadherin 2 or N-cadherin
	FN1	fibronectin 1
	MAP1B	microtubule associated protein 1B
	MSN	moesin
	SNAI1	snail family zinc finger 1
	SNAI2	snail family zinc finger 2
	SPARC	secreted protein acidic and cysteine rich
	TWIST1	twist family bHLH transcription factor 1
	VCAN	versican
	VIM	vimentin
	WNT5A	wingless-type MMTV integration site family member 5A
	WNT5B	wingless-type MMTV integration site family member 5B
	ZEB1	zinc finger E-box binding homeobox 1
EMT-down -regulated	*CDH1*	cadherin 2 or E-cadherin
	DSP	desmoplakin
	EZR	ezrin
	CLDN3	claudin 3
	CLDN4	claudin 4
	CLDN7	claudin 7
EGFR family	*EGFR/ERBB1*	epidermal growth factor receptor
	HER2/ERBB2	human epidermal growth factor receptor 2
	HER3/ERBB3	human epidermal growth factor receptor 3
	HER4/ERBB4	human epidermal growth factor receptor 4

Supplementary References

1. Debnath J, Muthuswamy SK, Brugge JS. Morphogenesis and oncogenesis of MCF-10A mammary epithelial acini grown in three-dimensional basement membrane cultures. *Methods* **30**, 256-268 (2003).
2. Pons T, Uyeda HT, Medintz IL, Mattoussi H. Hydrodynamic dimensions, electrophoretic mobility, and stability of hydrophilic quantum dots. *The Journal of Physical Chemistry B* **110**, 20308-20316 (2006).
3. Hendriks CL, Van Vliet L, Rieger B, van Kempen G, van Ginkel M. DIPimage: a scientific image processing toolbox for MATLAB. *Quantitative Imaging Group, Faculty of Applied Sciences, Delft University of Technology, Delft, The Netherlands*, (1999).
4. Andrews NL*, et al.* Actin restricts Fcϵ RI diffusion and facilitates antigen-induced receptor immobilization. *Nature cell biology* **10**, 955-963 (2008).
5. Liu Y-L*, et al.* Segmentation of 3D Trajectories Acquired by TSUNAMI Microscope: An Application to EGFR Trafficking. *Biophysical Journal* **111**, 2214-2227 (2016).
6. Arndt-Jovin DJ*, et al.* In vivo cell imaging with semiconductor quantum dots and noble metal nanodots. In: *Colloidal Quantum Dots for Biomedical Applications* (ed^(eds). International Society for Optics and Photonics (2006).
7. Dahan M, Levi S, Luccardini C, Rostaing P, Riveau B, Triller A. Diffusion dynamics of glycine receptors revealed by single-quantum dot tracking. *Science* **302**, 442-445 (2003).
8. Saxton MJ. Lateral Diffusion in an Archipelago - Single-Particle Diffusion. *Biophysical Journal* **64**, 1766-1780 (1993).
9. Martin DS, Forstner MB, Käs JA. Apparent subdiffusion inherent to single particle tracking. *Biophysical Journal* **83**, 2109-2117 (2002).
10. Saxton MJ, Jacobson K. Single-particle tracking: applications to membrane dynamics. *Annual Review of Biophysics and Biomolecular Structure* **26**, 373-399 (1997).
11. Kusumi A, Sako Y, Yamamoto M. Confined lateral diffusion of membrane receptors as studied by single particle tracking (nanovid microscopy). Effects of calcium-induced differentiation in cultured epithelial cells. *Biophysical journal* **65**, 2021-2040 (1993).
12. Clausen MP, Lagerholm BC. Visualization of plasma membrane compartmentalization by high-speed quantum dot tracking. *Nano letters* **13**, 2332-2337 (2013).
13. Daumas F, Destainville N, Millot C, Lopez A, Dean D, Salome L. Confined diffusion without fences of a G-protein-coupled receptor as revealed by single particle tracking. *Biophysical Journal* **84**, 356-366 (2003).
14. Di Rienzo C, Gratton E, Beltram F, Cardarelli F. Fast spatiotemporal correlation spectroscopy to determine protein lateral diffusion laws in live cell membranes. *Proceedings of the National Academy of Sciences* **110**, 12307-12312 (2013).
15. Prat A*, et al.* Phenotypic and molecular characterization of the claudin-low intrinsic subtype of breast cancer. *Breast cancer research* **12**, R68 (2010).
16. Lim E*, et al.* Aberrant luminal progenitors as the candidate target population for basal tumor development in BRCA1 mutation carriers. *Nature medicine* **15**, 907 (2009).
17. Marron JS, Todd MJ, Ahn J. Distance-weighted discrimination. *Journal of the American Statistical Association* **102**, 1267-1271 (2007).
18. Johnson NL, Kotz S, Balakrishnan N. Lognormal distributions. *Continuous univariate distributions* **1**, 207-227 (1994).
19. Osmulski P*, et al.* Nanomechanical biomarkers of single circulating tumor cells for detection of castration resistant prostate cancer. *The Prostate* **74**, 1297-1307 (2014).
20. Radmacher M, Fritz M, Kacher CM, Cleveland JP, Hansma PK. Measuring the viscoelastic properties of human platelets with the atomic force microscope. *Biophysical journal* **70**, 556-567 (1996).

21. Calzado-Martín A, Encinar M, Tamayo J, Calleja M, San Paulo A. Effect of actin organization on the stiffness of living breast cancer cells revealed by peak-force modulation atomic force microscopy. *ACS nano* **10**, 3365-3374 (2016).
22. Shin D, Athanasiou K. Cytoindentation for obtaining cell biomechanical properties. *Journal of Orthopaedic Research* **17**, 880-890 (1999).
23. Puig-de-Morales-Marinkovic M, Turner KT, Butler JP, Fredberg JJ, Suresh S. Viscoelasticity of the human red blood cell. *American Journal of Physiology-Cell Physiology* **293**, C597-C605 (2007).
24. Wang N, Ingber DE. Probing transmembrane mechanical coupling and cytomechanics using magnetic twisting cytometry. *Biochemistry and Cell Biology* **73**, 327-335 (1995).
25. Mason T, Ganesan K, Van Zanten J, Wirtz D, Kuo S. Particle tracking microrheology of complex fluids. *Physical Review Letters* **79**, 3282 (1997).
26. Guo M*, et al.* Probing the stochastic, motor-driven properties of the cytoplasm using force spectrum microscopy. *Cell* **158**, 822-832 (2014).
27. Wirtz D. Particle-tracking microrheology of living cells: principles and applications. *Annual review of biophysics* **38**, 301-326 (2009).
28. Tan JL, Tien J, Pirone DM, Gray DS, Bhadriraju K, Chen CS. Cells lying on a bed of microneedles: an approach to isolate mechanical force. *Proceedings of the National Academy of Sciences* **100**, 1484-1489 (2003).
29. Paszek MJ*, et al.* Tensional homeostasis and the malignant phenotype. *Cancer cell* **8**, 241-254 (2005).
30. Bao G, Suresh S. Cell and molecular mechanics of biological materials. *Nature materials* **2**, 715 (2003).
31. Hochmuth RM. Micropipette aspiration of living cells. *Journal of biomechanics* **33**, 15-22 (2000).
32. Dao M, Lim CT, Suresh S. Mechanics of the human red blood cell deformed by optical tweezers. *Journal of the Mechanics and Physics of Solids* **51**, 2259-2280 (2003).
33. Zhang H, Liu K-K. Optical tweezers for single cells. *Journal of The Royal Society Interface* **5**, 671-690 (2008).
34. Guck J*, et al.* Optical deformability as an inherent cell marker for testing malignant transformation and metastatic competence. *Biophysical journal* **88**, 3689-3698 (2005).
35. Hou HW, Li Q, Lee G, Kumar A, Ong C, Lim CT. Deformability study of breast cancer cells using microfluidics. *Biomedical microdevices* **11**, 557-564 (2009).
36. Gossett DR*, et al.* Hydrodynamic stretching of single cells for large population mechanical phenotyping. *Proceedings of the National Academy of Sciences* **109**, 7630-7635 (2012).
37. Network TPS-OC. A physical sciences network characterization of non-tumorigenic and metastatic cells. *Scientific reports* **3**, (2013).
38. Kramer N*, et al.* In vitro cell migration and invasion assays. *Mutation Research/Reviews in Mutation Research* **752**, 10-24 (2013).
39. Neve RM*, et al.* A collection of breast cancer cell lines for the study of functionally distinct cancer subtypes. *Cancer cell* **10**, 515-527 (2006).
40. Prat A, Perou CM. Deconstructing the molecular portraits of breast cancer. *Molecular oncology* **5**, 5-23 (2011).
41. Kao J*, et al.* Molecular profiling of breast cancer cell lines defines relevant tumor models and provides a resource for cancer gene discovery. *PloS one* **4**, e6146 (2009).
42. Subik K*, et al.* The expression patterns of ER, PR, HER2, CK5/6, EGFR, Ki-67 and AR by immunohistochemical analysis in breast cancer cell lines. *Breast cancer: basic and clinical research* **4**, 35 (2010).
43. Oberst M*, et al.* Matriptase and HAI-1 are expressed by normal and malignant epithelial cells in vitro and in vivo. *The American journal of pathology* **158**, 1301-1311 (2001).
44. Cappellen D, Schlange T, Bauer M, Maurer F, Hynes NE. Novel c-MYC target genes mediate differential effects on cell proliferation and migration. *EMBO Rep* **8**, 70-76 (2007).

45. Marshall AM, Pai VP, Sartor MA, Horseman ND. In vitro multipotent differentiation and barrier function of a human mammary epithelium. *Cell Tissue Res* **335**, 383-395 (2009).
46. Hook KE*, et al.* An integrated genomic approach to identify predictive biomarkers of response to the aurora kinase inhibitor PF-03814735. *Mol Cancer Ther* **11**, 710-719 (2012).
47. Odrowaz Z, Sharrocks AD. The ETS transcription factors ELK1 and GABPA regulate different gene networks to control MCF10A breast epithelial cell migration. *PLoS One* **7**, e49892 (2012).
48. Odrowaz Z, Sharrocks AD. ELK1 uses different DNA binding modes to regulate functionally distinct classes of target genes. *PLoS genetics* **8**, e1002694 (2012).
49. Bourdeau V, Deschenes J, Laperriere D, Aid M, White JH, Mader S. Mechanisms of primary and secondary estrogen target gene regulation in breast cancer cells. *Nucleic Acids Res* **36**, 76-93 (2008).
50. Kohlmann A*, et al.* An international standardization programme towards the application of gene expression profiling in routine leukaemia diagnostics: the Microarray Innovations in LEukemia study prephase. *British journal of haematology* **142**, 802-807 (2008).
51. Carroll JS*, et al.* Genome-wide analysis of estrogen receptor binding sites. *Nature genetics* **38**, 1289-1297 (2006).
52. Lin CY*, et al.* Whole-genome cartography of estrogen receptor alpha binding sites. *PLoS genetics* **3**, e87 (2007).
53. Lin Z, Reierstad S, Huang CC, Bulun SE. Novel estrogen receptor-alpha binding sites and estradiol target genes identified by chromatin immunoprecipitation cloning in breast cancer. *Cancer Res* **67**, 5017-5024 (2007).
54. Musgrove EA*, et al.* Identification of functional networks of estrogen- and c-Myc-responsive genes and their relationship to response to tamoxifen therapy in breast cancer. *PLoS One* **3**, e2987 (2008).
55. Stockwin LH, Yu SX, Stotler H, Hollingshead MG, Newton DL. ARC (NSC 188491) has identical activity to Sangivamycin (NSC 65346) including inhibition of both P-TEFb and PKC. *Bmc Cancer* **9**, 63 (2009).
56. Chen JL*, et al.* Lactic acidosis triggers starvation response with paradoxical induction of TXNIP through MondoA. *PLoS genetics* **6**, e1001093 (2010).
57. Barretina J*, et al.* The Cancer Cell Line Encyclopedia enables predictive modelling of anticancer drug sensitivity. *Nature* **483**, 603-607 (2012).
58. Krupp M, Itzel T, Maass T, Hildebrandt A, Galle PR, Teufel A. CellLineNavigator: a workbench for cancer cell line analysis. *Nucleic Acids Res* **41**, D942-948 (2013).
59. Nelson ER*, et al.* 27-Hydroxycholesterol links hypercholesterolemia and breast cancer pathophysiology. *Science* **342**, 1094-1098 (2013).
60. Pfister TD*, et al.* Topoisomerase I levels in the NCI-60 cancer cell line panel determined by validated ELISA and microarray analysis and correlation with indenoisoquinoline sensitivity. *Mol Cancer Ther* **8**, 1878-1884 (2009).
61. Wang L*, et al.* Cell cycle gene networks are associated with melanoma prognosis. *PLoS One* **7**, e34247 (2012).
62. Larsson O*, et al.* Distinct perturbation of the translatome by the antidiabetic drug metformin. *Proceedings of the National Academy of Sciences of the United States of America* **109**, 8977-8982 (2012).
63. Vivanco I*, et al.* Identification of the JNK signaling pathway as a functional target of the tumor suppressor PTEN. *Cancer cell* **11**, 555-569 (2007).
64. Shankar J, Messenberg A, Chan J, Underhill TM, Foster LJ, Nabi IR. Pseudopodial actin dynamics control epithelial-mesenchymal transition in metastatic cancer cells. *Cancer Res* **70**, 3780-3790 (2010).
65. Appaiah H, Bhat-Nakshatri P, Mehta R, Thorat M, Badve S, Nakshatri H. ITF2 is a target of CXCR4 in MDA-MB-231 breast cancer cells and is associated with reduced survival in estrogen receptor-negative breast cancer. *Cancer biology & therapy* **10**, 600-614 (2010).